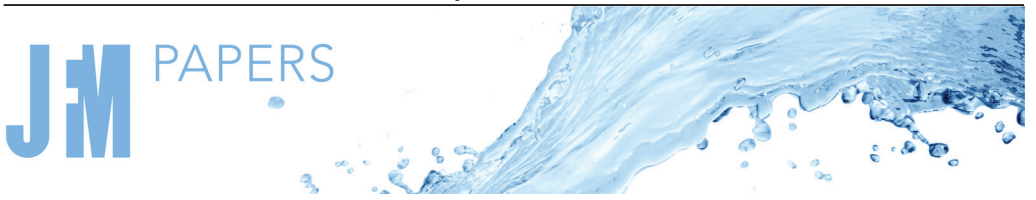
J. Fluid Mech. (2021), *vol*. 926, A16, doi:10.1017/jfm.2021.717



An adjoint approach for computing the receptivity of the rotating disc boundary layer to surface roughness

Christian Thomas[1],† **and Christopher Davies**[2]

[1]Department of Mathematics and Statistics, Macquarie University, NSW 2109, Australia

[2]School of Engineering, University of Leicester, University Road, Leicester LE1 7RH, UK

(Received 19 October 2020; revised 29 June 2021; accepted 10 August 2021)

An adjoint approach is developed to compute the receptivity of the rotating disc boundary layer to surface roughness. The adjoint linearised Navier–Stokes equations, in cylindrical coordinates, are derived and receptivity characteristics are computed for a broad range of azimuthal mode numbers using a fully equivalent velocity–vorticity formulation. For each set of flow conditions (i.e. azimuthal mode number), the adjoint method only requires that the linear and adjoint solutions be computed once. Thus, the adjoint approach offers significant computational and time advantages over alternative receptivity schemes (i.e. direct linearised Navier–Stokes) as they can be used to instantaneously compute the receptivity of boundary layer disturbances to many environmental mechanisms. Stationary cross-flow disturbances are established by randomly distributed surface roughness that is periodic in the azimuthal direction and modelled via a linearisation of the no-slip condition on the disc surface. Each roughness distribution is scaled on its respective root-mean-square. A Monte-Carlo type uncertainty quantification analysis is performed, whereby mean receptivity amplitudes are computed by averaging over many thousands of roughness realisations with variable length and wavelength filters. The amplitude of the cross-flow instability is significantly larger for roughness distributions near the conditions for neutral linear instability, while roughness elements radially outboard have a negligible effect on the receptivity process. Furthermore, receptivity increases sharply for roughness distributions that encompass wavelength scales equivalent to that associated with the cross-flow instability. Finally, mean receptivity characteristics are used to predict the radial range that stationary cross-flow vortices achieve amplitudes sufficient to invalidate the linear stability assumptions.

Key words: boundary layer receptivity, boundary layer stability, absolute/convective instability

† Email address for correspondence: christian.thomas@mq.edu.au

© The Author(s), 2021. Published by Cambridge University Press

https://doi.org/10.1017/jfm.2021.717 Published online by Cambridge University Press

1. Introduction

The initial stage of the laminar–turbulent transition process is known as receptivity (Morkovin 1969), whereby environmental disturbances transform into perturbations within the boundary layer. Such environmental disturbances can include free-stream noise, vortex structures and surface roughness. Excellent reviews on the receptivity process and boundary layer transition mechanisms are presented by Saric, Reed & Kerschen (2002) and Saric, Reed & White (2003).

The receptivity process establishes the initial conditions of the boundary layer disturbance, including the disturbance amplitude, frequency and phase. The amplitude of the initial fluctuation dictates the transition path to turbulence. If the initial perturbations are small, the growth (or decay) of the disturbances can be described using linear stability theory. Depending on the geometry of the body and the flow conditions, two- or three-dimensional disturbances may be excited that govern the preliminary stages of the laminar–turbulent transition process. For instance, Tollmien–Schlichting (TS) waves develop on a flat surface or an unswept wing, while cross-flow vortices grow within the boundary layer on a swept wing or rotating disc (von Kármán 1921; Lingwood & Alfredsson 2015). Linear disturbances can be decomposed as

$$\boldsymbol{q}(\boldsymbol{x}, t) = A\hat{\boldsymbol{q}}(\boldsymbol{x}, t), \tag{1.1}$$

where $\hat{\boldsymbol{q}}$ encompasses the growth (or decay) rate of the perturbation that is governed by the flow conditions, including the Reynolds number of the flow, spatial wavelength and temporal periodicity. (Here $\boldsymbol{x}$ represents the spatial coordinates and t time.) The disturbance amplitude A accounts for the receptivity to the environmental forcing; free-stream effects or surface roughness can vary significantly from one case to another, establishing different disturbance amplitudes that bring about considerable variations in the onset of the latter stages of transition. As the disturbance grows to larger amplitudes, linear stability theory becomes inappropriate, and nonlinear processes and secondary instabilities (amongst other instability mechanisms) emerge that lead to the breakdown of the flow to a turbulent state.

Goldstein (1983) identified a receptivity mechanism, whereby an acoustic disturbance (i.e. sound wave) near the leading edge of a flat plate interacts with the flow to establish a TS wave. Another receptivity mechanism was identified independently by Ruban (1984) and Goldstein (1985) that involves a sound wave interacting with a disturbance generated by surface roughness. Following these seminal receptivity investigations, voluminous studies (only a few are cited below) have been undertaken on boundary layer receptivity, including Crouch (1992*a*,*b*), Choudhari & Streett (1992) and Choudhari (1993), who modelled acoustic forcing over a flat plate with surface roughness. Additionally, Wu (2001*a*,*b*) applied asymptotic theory to distributed and localised roughness in the presence of vortical and acoustic waves.

Choudhari (1994) modelled the receptivity of swept wing boundary layers (Falkner–Skan–Cooke flows), whereby stationary and non-stationary cross-flow vortices were excited by a spanwise-periodic roughness distribution. Using a compressible linearised Navier–Stokes solver, Collis & Lele (1999) found that surface curvature and non-parallel effects played a significant role in the receptivity process along the leading edge of a swept wing. Later, Schrader and co-workers modelled the receptivity of a swept wing leading edge by coupling free-stream turbulence and surface roughness (Schrader, Brandt & Henningson 2009; Schrader, Amin & Brandt 2010).

Several experiments on a swept wing were undertaken by the Saric group, in which cross-flow disturbances were excited by localised roughness elements (Reibert *et al.*

https://doi.org/10.1017/jfm.2021.717 Published online by Cambridge University Press

1996; Saric, Carrillo & Reibert 1998; Radeztsky, Reibert & Saric 1999). In particular, it was noted by Radeztsky *et al.* (1999) that receptivity is most enhanced by roughness elements located near the onset of unstable behaviour. Numerical methods were employed by Ng & Crouch (1999) in an attempt to replicate the Saric experiments. Using a local parallel flow assumption, they obtained qualitatively similar results as that found experimentally. More recently, Tempelmann *et al.* (2012*b*) employed direct numerical simulations (DNS) and parabolised stability equations (PSE) to study the receptivity of a swept wing to localised roughness elements, with the objective to reproduce the wind tunnel experiments performed by the Saric group. In all cases modelled, DNS and PSE cross-flow amplitudes were smaller than the equivalent experimental disturbance measurements. It was suggested that uncertainties in the experimental set-up were possibly responsible for these differences.

This paper is concerned with the receptivity of the rotating disc boundary layer to randomly distributed surface roughness, which is the archetypal model for the study of three-dimensional instability mechanisms that trigger laminar–turbulent transition. The flow on a rotating disc is formed when a planar solid surface is rotated, with a constant angular velocity, that drives the motion of the otherwise still fluid immediately above it. This particular flow has been of fundamental interest to the fluid dynamics community throughout much of the twentieth and twenty-first centuries, with the foundational study undertaken by von Kármán (1921). A review by Lingwood & Alfredsson (2015) provides an extensive overview of the numerous investigations that have been carried out on the rotating disc using theoretical, numerical and experimental methods. The seminal experimental and theoretical study by Gregory, Stuart & Walker (1955) revealed that the inviscid cross-flow instability appears as stationary spiral vortices on the rotating disc. In addition to cross-flow disturbances, the rotating disc is susceptible to at least two other forms of instability. The first of these instabilities is viscous and is a direct consequence of the Coriolis forces present in rotating boundary layers (Faller & Kaylor 1966; Malik 1986), while the second instability is a spatially damped mode that propagates radially inwards (Mack 1985).

In their china-clay visualisation experiments, Gregory *et al.* (1955) observed cross-flow disturbances as 28–32 vortices that spiralled radially outwards at an angle of 14°. The number of cross-flow vortices is directly related to the integer-valued azimuthal mode number n that represents the periodicity of the disturbance in the azimuthal direction. Similar observations were made in later experimental studies by Kobayashi, Kohama & Takamadate (1980), Malik, Wilkinson & Orszag (1981), Kohama (1984) and Wilkinson & Malik (1985). The onset of these stationary cross-flow vortices was observed experimentally for a Reynolds number $Re_c < 300$ (Kobayashi *et al.* 1980; Malik *et al.* 1981) and confirmed as $Re_c \approx 286$ using linear stability theory by Malik *et al.* (1981) and Lingwood (1995), amongst many others. Moreover, Siddiqui *et al.* (2013) observed that those stationary perturbations with an azimuthal mode number near $n = 30$ developed with the largest spatial growth. (A formal definition for the Reynolds number Re is given below in (2.7).)

An absolute form of instability was discovered by Lingwood (1995) using the Briggs (1964) pinch-point criterion, and was shown to result from the coalescence of the cross-flow instability (Gregory *et al.* 1955) and the spatially damped mode found by Mack (1985). More dangerous than the convectively unstable cross-flow mode, Lingwood (1995) identified the critical Reynolds number for absolute instability as $Re_a = 510$ (later corrected to $Re_a = 507$ by Lingwood 1997) for an azimuthal mode number $n = 68$. The linear stability analysis undertaken by Lingwood (1995) was based on a local theory, which was achieved by imposing a spatially homogeneous flow approximation. This is

https://doi.org/10.1017/jfm.2021.717 Published online by Cambridge University Press

often termed the parallel flow approximation, whereby the radial dependence of the base flow is ignored.

Davies & Carpenter (2003) undertook a numerical investigation of the radially dependent inhomogeneous flow over an infinite rotating disc and showed that absolute instability was not sufficient for a disturbance to become globally linearly unstable. Instead, for azimuthal mode numbers n near the critical conditions for absolute instability, convective characteristics dominated the global disturbance development. However, a subsequent study by Thomas & Davies (2018) found that a form of global linear instability can occur, although such behaviour only arises for azimuthal mode numbers significantly greater than that associated with the onset of absolute instability that were the primary focus of the earlier investigation. While absolute instability is a necessary condition for the onset of global linear instability to occur, it is not a sufficient condition. Generally, the region of absolute instability must exceed some threshold size for global linear instability to ensue (Chomaz, Huerre & Redekopp 1988; Huerre & Monkewitz 1990). In particular, for the flow on a rotating disc, the radial extent of absolute instability increases as the azimuthal mode number n increases. Thomas & Davies (2018) found that, for $n \gtrapprox 83$, globally linearly unstable behaviour emerges that is characterised by a stronger than exponential temporal growth. Furthermore, Thomas and Davies utilised solutions of the Ginzburg–Landau equation (Hunt & Crighton 1991) to show that the onset of global linear instability can be predicted using local stability characteristics based on the homogeneous flow approximation. The results of Thomas and Davies indicate that the infinite rotating disc is stable for small Reynolds numbers Re and azimuthal mode numbers n. For larger Re and n, regions of local convective instability (such as cross-flow vortices) and absolute instability emerge, but globally linearly unstable behaviour only develops for sufficiently large azimuthal mode numbers. Further studies have shown that this behaviour is ubiquitous across the family of rotating boundary layers, including cones in a quiescent medium and discs with roughness modelled via the partial-slip boundary condition (Thomas & Davies 2019; Thomas, Stephen & Davies 2020).

Experimental observations indicate that transition to turbulence in the rotating disc boundary layer is highly reproducible with Reynolds numbers $500 \leqslant Re \leqslant 566$ quoted in the literature. For instance, Gregory *et al.* (1955) observed transition for $Re = 533$, while Malik *et al.* (1981) and Kobayashi *et al.* (1980) indicate that transition sets in for $513 < Re < 526$ and $Re = 566$, respectively. More recently, Lingwood (1996) suggests that transition on a clean disc occurs for Reynolds numbers $Re = 513 \pm 3\,\%$, while Othman & Corke (2006) observed transition about $Re = 539$. A comprehensive list of the many experimental investigations undertaken on the rotating disc and transition Reynolds numbers is given by Imayama, Alfredsson & Lingwood (2013); see table 1 of their paper.

Since absolute instability and transition to turbulence occur within the same band of Reynolds numbers, Lingwood (1996) suggested that the absolutely unstable mechanism is the primary cause for the breakdown of the laminar flow. Several recent investigations on a rotating disc of finite radius suggest that absolute instability can establish globally unstable behaviour if disc edge effects are accounted for (Healey 2010; Imayama *et al.* 2013; Pier 2013; Appelquist *et al.* 2015, 2016; Lee *et al.* 2017, 2018). Additionally, Pier (2003) suggests that a secondary absolute instability develops near the primary absolute instability, providing an alternative route to turbulence. Meanwhile, the discovery by Thomas & Davies (2018) that a form of global linear instability develops for sufficiently large azimuthal mode numbers n may provide additional support to Lingwood's conclusions. However, there does not appear to be any evidence for these large n modes in the available experimental literature. This does not imply that these globally unstable disturbances do not exist, but that other faster growing instabilities (such as the cross-flow

https://doi.org/10.1017/jfm.2021.717 Published online by Cambridge University Press

instability) may prevent their development. Cross-flow disturbances (both stationary and travelling) grow rapidly and can achieve exponential growth factors $N \in [7 : 11]$ within the range of Reynolds numbers that transition is observed experimentally (Thomas & Davies 2018). Hence, cross-flow vortices may still be the primary mechanism for laminar–turbulent transition in the rotating disc boundary layer.

Imayama *et al.* (2013) remark that the onset of transition in experiments is dependent on the definition for transition. For instance, Lingwood (1996) based her observations for transition on the onset of nonlinearity, while Othman & Corke (2006) based it on the deformation of the laminar flow profile. (Table 3 of Imayama *et al.* (2013) provides an overview of the interpretations for transition in experiments.) Nevertheless, independent of the definition for transition, there is a clear and marked region on the disc that transition occurs. Additionally, it is very difficult to eliminate stationary cross-flow vortices in experiments, even for the flow over a polished disc; unavoidable surface roughness will inevitably excite stationary cross-flow disturbances (Imayama, Alfredsson & Lingwood 2016). Thus, the route to transition is dependent on the roughness height. Wilkinson & Malik (1985) found that transition occurred for $521 < Re < 530$ on a rough disc, while transition on a clean disc was delayed to $543 < Re < 556$. Imayama *et al.* (2016) experimentally modelled surface roughness effects, whereby artificial roughness elements were placed on the surface of an otherwise clean disc. As expected, transition occurred earlier on the rough disc, with very little surface roughness needed to trigger the strong growth of unstable stationary cross-flow disturbances. Thus, transition occurred via a convective route. However, in addition to the stationary cross-flow instability, travelling disturbances were observed on the clean disc. It was suggested that this is evidence for absolute instability, and thus, transition to turbulence occurs via an absolute route. On the other hand, Appelquist *et al.* (2018) numerically excited stationary cross-flow disturbances via surface roughness elements of variable amplitude, and traced their development through the linear stage, nonlinear saturation and finally transition to turbulence. In all instances simulated, the primary instability was convectively unstable, before nonlinear effects and secondary instabilities formed.

In experimental apparatus, a disc is deemed to be rough when an artificial roughness is fixed to the disc surface. A disc is then described as clean if it is polished to a certain threshold level. In Othman & Corke (2006) the disc surface was polished to a 2 μm finish, while the natural surface roughness was less than 1 μm in Imayama, Alfredsson & Lingwood (2012), Imayama *et al.* (2013), Imayama, Alfredsson & Lingwood (2014) and Imayama *et al.* (2016). However, even for clean discs natural surface roughness still occurs and will inevitably excite stationary cross-flow disturbances, albeit at a lower initial amplitude. Furthermore, the size and shape of the roughness will be specific to each disc, leading to both different receptivity amplitudes and routes to turbulence. Quantifying this effect and computing the receptivity amplitude can be computationally expensive using the linear Navier–Stokes (LNS) equations. Indeed, computing mean receptivity characteristics for predicting the possible transition scenarios would require the LNS equations to be solved for many roughness realisations. Thus, the computational demands of an LNS based receptivity analysis can quickly escalate. However, such difficulties can be overcome using an adjoint based approach.

The adjoint linearised Navier–Stokes (ALNS) equations are both computationally and economically more efficient than other receptivity formulations (such as the LNS equations). They only require solutions to the LNS and ALNS equations to be computed once, after which they can be used to instantaneously predict the amplitude of the disturbance excited by many forms of external forcing. Hill (1995) derived the ALNS equations for the two-dimensional Blasius boundary layer and determined the sensitivity

https://doi.org/10.1017/jfm.2021.717 Published online by Cambridge University Press

of TS waves. Later, Airiau (2000) extended Hill's analysis to include non-parallel effects, while Dobrinsky & Collis (2000) and Dobrinsky (2002) employed adjoint methods to compute the receptivity of the family of Falkner–Skan flows. Adjoint formulations have been applied to many other flow systems and boundary layer instabilities (Luchini & Bottaro 1998; Pralits, Hanifi & Henningson 2002; Pralits & Hanifi 2003; Giannetti & Luchini 2006; Carpenter *et al.* 2010; Tempelmann, Hanifi & Henningson 2012*a*), with a review given by Luchini & Bottaro (2014).

Thomas, Mughal & Ashworth (2017) derived the compressible ALNS equations for the flow over a swept wing and undertook a Monte-Carlo type uncertainty quantification analysis. Many thousands of roughness distributions were randomly generated and the amplitude of stationary cross-flow vortices was computed to ascertain mean receptivity characteristics. Similar studies were undertaken by Mughal & Ashworth (2013) and Raposo, Mughal & Ashworth (2018) using an LNS scheme.

In this investigation we derive for the first time, the ALNS equations in cylindrical coordinates for the rotating disc boundary layer. An extensive receptivity study is undertaken, whereby stationary cross-flow vortices are established by many randomly generated surface roughnesses. Mean receptivity characteristics, based on the root-mean-square (r.m.s.) of the surface roughness, are then used to predict the radial location that the stationary cross-flow instability attains amplitudes sufficient to invalidate the linear stability assumptions and bring about nonlinear effects and the latter stages of the laminar–turbulent transition process.

The remainder of this paper is outlined as follows. In the subsequent section the undisturbed flow is described. In § 3 the ALNS equations in cylindrical coordinates are derived. The velocity–vorticity form of the ALNS equations are presented in § 4 based on the formulation of Davies & Carpenter (2001). The receptivity of the rotating disc boundary layer to surface roughness is discussed in § 5, with conclusions given in § 6.

2. Undisturbed flow

A disc of infinite radius rotates beneath an infinite body of incompressible fluid at a constant angular velocity Λ^* about the vertical axis that passes through the centre of the disc. The modelling is carried out in cylindrical polar coordinates, where r^*, θ and z^* denote the radial, azimuthal and wall-normal directions, respectively. (Here an asterisk denotes dimensional quantities.) In what follows, all quantities are defined in the frame of reference that rotates with the disk.

The Navier–Stokes equations, in cylindrical coordinates, are defined as

$$\frac{\partial U_r^*}{\partial t^*} + (\boldsymbol{U^*}\cdot\boldsymbol{\nabla}^*)U_r^* - \frac{U_\theta^{*2}}{r^*} - 2\Lambda^* U_\theta^* - \Lambda^{*2} r^* = -\frac{1}{\rho^*}\frac{\partial P^*}{\partial r^*} + \nu^*\left(\boldsymbol{\nabla}^{*2}U_r^* - \frac{U_r^*}{r^{*2}} - \frac{2}{r^{*2}}\frac{\partial U_\theta^*}{\partial\theta}\right), \tag{2.1a}$$

$$\frac{\partial U_\theta^*}{\partial t^*} + (\boldsymbol{U^*}\cdot\boldsymbol{\nabla}^*)U_\theta^* + \frac{U_\theta^* U_r^*}{r^*} + 2\Lambda^* U_r^* = -\frac{1}{r^*\rho^*}\frac{\partial P^*}{\partial\theta} + \nu^*\left(\boldsymbol{\nabla}^{*2}U_\theta^* - \frac{U_\theta^*}{r^{*2}} + \frac{2}{r^{*2}}\frac{\partial U_r^*}{\partial\theta}\right), \tag{2.1b}$$

https://doi.org/10.1017/jfm.2021.717 Published online by Cambridge University Press

$$\frac{\partial U_z^*}{\partial t^*} + (\boldsymbol{U}^* \cdot \boldsymbol{\nabla}^*) U_z^* = -\frac{1}{\rho^*}\frac{\partial P^*}{\partial z^*} + \nu^* \boldsymbol{\nabla}^{*2} U_z^*, \tag{2.1c}$$

$$\frac{1}{r^*}\frac{\partial (r^* U_r^*)}{\partial r^*} + \frac{1}{r^*}\frac{\partial U_\theta^*}{\partial \theta} + \frac{\partial U_z^*}{\partial z^*} = 0, \tag{2.1d}$$

where

$$\boldsymbol{U}^* \cdot \boldsymbol{\nabla}^* = U_r^* \frac{\partial}{\partial r^*} + \frac{U_\theta^*}{r^*}\frac{\partial}{\partial \theta} + U_z^* \frac{\partial}{\partial z^*} \tag{2.2a}$$

and

$$\boldsymbol{\nabla}^{*2} = \frac{\partial^2}{\partial r^{*2}} + \frac{1}{r^*}\frac{\partial}{\partial r^*} + \frac{1}{r^{*2}}\frac{\partial^2}{\partial \theta^2} + \frac{\partial^2}{\partial z^{*2}}. \tag{2.2b}$$

The kinematic viscosity and density of the fluid are denoted by ν^* and $\rho*$, while $\boldsymbol{U}^* = (U_r^*, U_\theta^*, U_z^*)$ and P^* represent the respective dimensional velocity and pressure fields. Boundary conditions on the disc surface are defined as

$$U_r^* = U_\theta^* = U_z^* = 0 \quad \text{on } z^* = 0, \tag{2.3a–c}$$

and in the far field

$$U_r^* \to 0 \quad \text{and} \quad U_\theta^* \to -r^* \Lambda^* \quad \text{as } z^* \to \infty. \tag{2.3d,e}$$

The undisturbed flow field is established using the von Kármán (1921) similarity variables

$$\boldsymbol{U}^* = \left(r^* \Lambda^* F(z), r^* \Lambda^* G(z), \delta^* \Lambda^* H(z)\right) \quad \text{and} \quad P^* = \rho^* \nu^* \Lambda^* P(z), \tag{2.4a,b}$$

where F, G and H represent the non-dimensional velocity profiles along the three coordinate directions. The non-dimensional pressure field is denoted P and $\delta^* = \sqrt{\nu^*/\Lambda^*}$ represents the constant boundary layer thickness used here to scale units of length: $r = r^*/\delta^*$ and $z = z^*/\delta^*$. On substituting (2.4) into the Navier–Stokes equations (2.1), the following system of ordinary differential equations for F, G, H and P is derived,

$$F'' = F^2 + F'H - (G+1)^2, \tag{2.5a}$$

$$G'' = 2F(G+1) + G'H, \tag{2.5b}$$

$$H'' = P' + HH', \tag{2.5c}$$

$$0 = 2F + H', \tag{2.5d}$$

which is solved subject to the boundary conditions

$$F = G = H = 0 \quad \text{on } z = 0 \tag{2.5e}$$

and

$$F \to 0 \quad \text{and} \quad G \to -1 \quad \text{as } z \to \infty. \tag{2.5f}$$

A prime denotes differentiation with respect to z. Figure 1 depicts the von Kármán velocity profiles F, G and H as functions of the wall-normal z-direction.

https://doi.org/10.1017/jfm.2021.717 Published online by Cambridge University Press

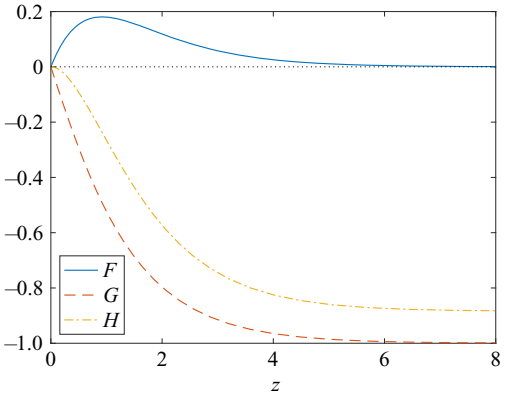


Figure 1. The von Kármán velocity profiles F, G and H.

Non-dimensionalising velocity and pressure on the respective scales $r_o^* \Lambda^*$ and $\rho^* r_o^{*2} \Lambda^{*2}$, the non-dimensional undisturbed velocity and pressure fields are given as

$$\boldsymbol{U_B}(r, z) = \left(\frac{r}{Re} F(z), \frac{r}{Re} G(z), \frac{1}{Re} H(z) \right) \quad \text{and} \quad P_B(z) = \frac{1}{Re^2} P(z), \tag{2.6a,b}$$

where the Reynolds number is defined as

$$Re = r_o^* / \delta^* \equiv r_o, \tag{2.7}$$

for a non-dimensional reference radius r_o.

3. Derivation of the ALNS equations

3.1. *Linearised Navier–Stokes equations*

The undisturbed flow (2.6) is perturbed by infinitesimally small disturbances, with the total velocity $\boldsymbol{U}$ and pressure P given as

$$\boldsymbol{U} = \boldsymbol{U_B} + \boldsymbol{u}, \quad P = P_B + p, \tag{3.1a,b}$$

where the velocity perturbation $\boldsymbol{u} = (u_r, u_\theta, u_z)$. Substituting (3.1) into the Navier–Stokes equations and linearising with respect to the perturbation $\boldsymbol{q} = (\boldsymbol{u}, p)$ gives the LNS system of equations

$$\begin{aligned} L_r(\boldsymbol{q}; \boldsymbol{U_B}, Re) = {} & \frac{\partial u_r}{\partial t} + \frac{rF}{Re} \frac{\partial u_r}{\partial r} + \frac{F}{Re} u_r + \frac{G}{Re} \frac{\partial u_r}{\partial \theta} + \frac{H}{Re} \frac{\partial u_r}{\partial z} + \frac{rF'}{Re} u_z \\ & - \frac{2(G+1)}{Re} u_\theta + \frac{\partial p}{\partial r} - \frac{1}{Re} \left(\left(\nabla^2 - \frac{1}{r^2} \right) u_r - \frac{2}{r^2} \frac{\partial u_\theta}{\partial \theta} \right) = 0, \end{aligned} \tag{3.2a}$$

$$\begin{aligned} L_\theta(\boldsymbol{q}; \boldsymbol{U_B}, Re) = {} & \frac{\partial u_\theta}{\partial t} + \frac{rF}{Re} \frac{\partial u_\theta}{\partial r} + \frac{F}{Re} u_\theta + \frac{G}{Re} \frac{\partial u_\theta}{\partial \theta} + \frac{H}{Re} \frac{\partial u_\theta}{\partial z} + \frac{rG'}{Re} u_z \\ & + \frac{2(G+1)}{Re} u_r + \frac{1}{r} \frac{\partial p}{\partial \theta} - \frac{1}{Re} \left(\left(\nabla^2 - \frac{1}{r^2} \right) u_\theta + \frac{2}{r^2} \frac{\partial u_r}{\partial \theta} \right) = 0, \end{aligned} \tag{3.2b}$$

$$L_z(\boldsymbol{q}; \boldsymbol{U_B}, Re) = \frac{\partial u_z}{\partial t} + \frac{rF}{Re} \frac{\partial u_z}{\partial r} + \frac{G}{Re} \frac{\partial u_z}{\partial \theta} + \frac{H}{Re} \frac{\partial u_z}{\partial z} + \frac{H'}{Re} u_z + \frac{\partial p}{\partial z} - \frac{1}{Re} \nabla^2 u_z = 0, \tag{3.2c}$$

https://doi.org/10.1017/jfm.2021.717 Published online by Cambridge University Press

$$\frac{1}{r}\frac{\partial (ru_r)}{\partial r} + \frac{1}{r}\frac{\partial u_\theta}{\partial \theta} + \frac{\partial u_z}{\partial z} = 0, \tag{3.2d}$$

where ∇^2 is the non-dimensional form of (2.2*b*). For convenience, we introduce the LNS operator $\boldsymbol{L} = (L_r, L_\theta, L_z)$.

The corresponding boundary conditions on the disc surface and in the far field are respectively given as

$$\boldsymbol{u} = \boldsymbol{0} \quad \text{on} \quad z = 0 \quad \text{and} \quad \boldsymbol{u} \to \boldsymbol{0} \quad \text{as } z \to \infty. \tag{3.3a,b}$$

3.2. *Adjoint linearised Navier–Stokes equations*

Formulating the Lagrange identity is key to deriving the ALNS system of equations. This is achieved by first introducing adjoint velocity $\tilde{\boldsymbol{u}} = (\tilde{u}_r, \tilde{u}_\theta, \tilde{u}_z)$ and pressure $\tilde{p}$ perturbation fields. The Lagrange identity is then derived by taking the inner product of the LNS equations (3.2) with $\tilde{\boldsymbol{q}} = (\tilde{\boldsymbol{u}}, \tilde{p})$, and integrating by parts to give

$$\underbrace{\boldsymbol{L}(\boldsymbol{q}; \boldsymbol{U_B}, Re) \cdot \tilde{\boldsymbol{u}} + \boldsymbol{\nabla} \cdot \boldsymbol{u}\tilde{p}}_{\text{Inner product of LNS } \&\tilde{\boldsymbol{q}}} + \underbrace{\boldsymbol{u} \cdot \tilde{\boldsymbol{L}}(\tilde{\boldsymbol{q}}; \boldsymbol{U_B}, Re) + p\boldsymbol{\nabla} \cdot \tilde{\boldsymbol{u}}}_{\text{Inner product of ALNS } \&\boldsymbol{q}}$$
$$= \underbrace{\frac{\partial}{\partial t}(\boldsymbol{u} \cdot \tilde{\boldsymbol{u}}) + \boldsymbol{\nabla} \cdot \boldsymbol{J}(\boldsymbol{q}, \tilde{\boldsymbol{q}})}_{\text{Bilinear concomitant}}, \tag{3.4}$$

where

$$\boldsymbol{u} \cdot \tilde{\boldsymbol{u}} = u_r\tilde{u}_r + u_\theta\tilde{u}_\theta + u_z\tilde{u}_z. \tag{3.5}$$

(Note that the integration along the radial direction is performed on a finite interval.)

The ALNS system of equations are then given by those expressions above the second underbrace in (3.4) that form an inner product with the linear perturbation $\boldsymbol{q} = (\boldsymbol{u}, p)$,

$$\tilde{L}_r(\tilde{\boldsymbol{q}}; \boldsymbol{U_B}, Re) = \frac{\partial \tilde{u}_r}{\partial t} + \frac{rF}{Re}\frac{\partial \tilde{u}_r}{\partial r} - \frac{F}{Re}\tilde{u}_r + \frac{G}{Re}\frac{\partial \tilde{u}_r}{\partial \theta} + \frac{H}{Re}\frac{\partial \tilde{u}_r}{\partial z}$$
$$- \frac{2(G+1)}{Re}\tilde{u}_\theta + \frac{\partial \tilde{p}}{\partial r} + \frac{1}{Re}\left(\left(\nabla^2 - \frac{1}{r^2}\right)\tilde{u}_r - \frac{2}{r^2}\frac{\partial \tilde{u}_\theta}{\partial \theta}\right) = 0, \tag{3.6a}$$

$$\tilde{L}_\theta(\tilde{\boldsymbol{q}}; \boldsymbol{U_B}, Re) = \frac{\partial \tilde{u}_\theta}{\partial t} + \frac{rF}{Re}\frac{\partial \tilde{u}_\theta}{\partial r} - \frac{F}{Re}\tilde{u}_\theta + \frac{G}{Re}\frac{\partial \tilde{u}_\theta}{\partial \theta} + \frac{H}{Re}\frac{\partial \tilde{u}_\theta}{\partial z}$$
$$+ \frac{2(G+1)}{Re}\tilde{u}_r + \frac{1}{r}\frac{\partial \tilde{p}}{\partial \theta} + \frac{1}{Re}\left(\left(\nabla^2 - \frac{1}{r^2}\right)\tilde{u}_\theta + \frac{2}{r^2}\frac{\partial \tilde{u}_r}{\partial \theta}\right) = 0, \tag{3.6b}$$

$$\tilde{L}_z(\tilde{\boldsymbol{q}}; \boldsymbol{U_B}, Re) = \frac{\partial \tilde{u}_z}{\partial t} + \frac{rF}{Re}\frac{\partial \tilde{u}_z}{\partial r} + \frac{G}{Re}\frac{\partial \tilde{u}_z}{\partial \theta} + \frac{H}{Re}\frac{\partial \tilde{u}_z}{\partial z} - \frac{rF'}{Re}\tilde{u}_r$$
$$- \frac{rG'}{Re}\tilde{u}_\theta - \frac{H'}{Re}\tilde{u}_z + \frac{\partial \tilde{p}}{\partial z} + \frac{1}{Re}\nabla^2\tilde{u}_z = 0, \tag{3.6c}$$

$$\frac{1}{r}\frac{\partial (r\tilde{u}_r)}{\partial r} + \frac{1}{r}\frac{\partial \tilde{u}_\theta}{\partial \theta} + \frac{\partial \tilde{u}_z}{\partial z} = 0, \tag{3.6d}$$

where the ALNS operator $\tilde{\boldsymbol{L}} = (\tilde{L}_r, \tilde{L}_\theta, \tilde{L}_z)$. Note that the viscous terms in the ALNS equations (3.6) are of the opposite sign to the equivalent terms in the LNS equations (3.2). Thus, the adjoint equations must be solved backwards in time.

https://doi.org/10.1017/jfm.2021.717 Published online by Cambridge University Press

The system of ALNS equations (3.6) are solved subject to an equivalent set of boundary conditions as imposed on the LNS system of equations (3.2),

$$\tilde{\boldsymbol{u}} = \boldsymbol{0} \quad \text{on} \quad z = 0 \quad \text{and} \quad \tilde{\boldsymbol{u}} \to \boldsymbol{0} \quad \text{as } z \to \infty. \tag{3.7a,b}$$

3.3. *Bilinear concomitant*

The operator $\boldsymbol{J} = (J_r, J_\theta, J_z)$, on the right-hand side of the Lagrange identity (3.4), represents the bilinear concomitant and is defined as

$$\begin{aligned} J_r(\boldsymbol{q}, \tilde{\boldsymbol{q}}) = {} & \frac{rF}{Re}\boldsymbol{u}\cdot\tilde{\boldsymbol{u}} + p\tilde{u}_r + u_r\tilde{p} \\ & + \frac{1}{Re}\left(u_r\frac{\partial\tilde{u}_r}{\partial r} - \tilde{u}_r\frac{\partial u_r}{\partial r} + u_\theta\frac{\partial\tilde{u}_\theta}{\partial r} - \tilde{u}_\theta\frac{\partial u_\theta}{\partial r} + u_z\frac{\partial\tilde{u}_z}{\partial r} - \tilde{u}_z\frac{\partial u_z}{\partial r}\right), \end{aligned} \tag{3.8a}$$

$$\begin{aligned} J_\theta(\boldsymbol{q}, \tilde{\boldsymbol{q}}) = {} & \frac{rG}{Re}\boldsymbol{u}\cdot\tilde{\boldsymbol{u}} + p\tilde{u}_\theta + u_\theta\tilde{p} \\ & + \frac{1}{rRe}\left(u_r\frac{\partial\tilde{u}_r}{\partial\theta} - \tilde{u}_r\frac{\partial u_r}{\partial\theta} + u_\theta\frac{\partial\tilde{u}_\theta}{\partial\theta} - \tilde{u}_\theta\frac{\partial u_\theta}{\partial\theta} + u_z\frac{\partial\tilde{u}_z}{\partial\theta}\right. \\ & \left. -\tilde{u}_z\frac{\partial u_z}{\partial\theta} + 2\left(u_\theta\tilde{u}_r - u_r\tilde{u}_\theta\right)\right), \end{aligned} \tag{3.8b}$$

$$\begin{aligned} J_z(\boldsymbol{q}, \tilde{\boldsymbol{q}}) = {} & \frac{H}{Re}\boldsymbol{u}\cdot\tilde{\boldsymbol{u}} + p\tilde{u}_z + u_z\tilde{p} \\ & + \frac{1}{Re}\left(u_r\frac{\partial\tilde{u}_r}{\partial z} - \tilde{u}_r\frac{\partial u_r}{\partial z} + u_\theta\frac{\partial\tilde{u}_\theta}{\partial z} - \tilde{u}_\theta\frac{\partial u_\theta}{\partial z} + u_z\frac{\partial\tilde{u}_z}{\partial z} - \tilde{u}_z\frac{\partial u_z}{\partial z}\right). \end{aligned} \tag{3.8c}$$

In the subsequent analysis, the $\boldsymbol{J}$-operator is utilised to establish a formula for predicting the receptivity amplitude of the stationary cross-flow instability excited by surface roughness.

3.4. *Normalisation*

Stationary cross-flow perturbations $\boldsymbol{q} = (\boldsymbol{u}, p)$ are assumed to be linear, infinitesimally small and of the general form

$$\boldsymbol{q}(r, \theta, z, t) = \hat{\boldsymbol{q}}(r, z)\mathrm{e}^{\mathrm{i}n\theta} \tag{3.9}$$

for an integer-valued azimuthal mode number n. Similarly, stationary adjoint perturbations $\tilde{\boldsymbol{q}} = (\tilde{\boldsymbol{u}}, \tilde{p})$ are assumed to be of the form

$$\tilde{\boldsymbol{q}}(r, \theta, z, t) = \tilde{\hat{\boldsymbol{q}}}(r, z)\mathrm{e}^{-\mathrm{i}n\theta}, \tag{3.10}$$

where a change in sign arises for the azimuthal mode number n as adjoint disturbances evolve in the spatially opposite sense to the LNS perturbation (3.9).

Assuming Fourier modes (3.9) and (3.10) are distinct modes of the respective systems (3.2) and (3.6), the Lagrange identity (3.4) can be reduced to the form

$$\frac{1}{r}\frac{\partial(rJ_r)}{\partial r} + \frac{\partial J_z}{\partial z} = 0, \tag{3.11}$$

where J_r and J_z are given explicitly in terms of the linear $\boldsymbol{q}$ and adjoint $\tilde{\boldsymbol{q}}$ perturbation fields. Furthermore, (3.11) can be simplified using the divergence theorem and by integrating over

https://doi.org/10.1017/jfm.2021.717 Published online by Cambridge University Press

the (r, z) domain to give

$$\mathcal{J}(r) = \int_0^\infty J_r(\boldsymbol{q}, \tilde{\boldsymbol{q}})\,\mathrm{d}z, \tag{3.12}$$

where the homogeneous boundary conditions (3.3) and (3.7) are implemented on the disc surface and in the far field. The quantity $\mathcal{J}$ is critical to the success of the adjoint method in predicting receptivity.

The linear perturbation $\boldsymbol{q}$ is normalised by setting

$$\max_z |u_\theta(r, z)| = 1 \quad \text{at } r = r_c, \tag{3.13a}$$

where r_c denotes the radial location that $\boldsymbol{q}$, with a fixed azimuthal mode number n, becomes unstable. The corresponding adjoint perturbation $\tilde{\boldsymbol{q}}$ is then normalised by fixing

$$\mathcal{J}(r) = 1 \quad \text{for all } r. \tag{3.13b}$$

Disturbance characteristics are normalised in this study on the azimuthal velocity perturbation field u_θ, rather than the radial velocity u_r or energy $K = (u_r^2 + u_\theta^2 + u_z^2)/2$. However, the subsequent analysis and conclusions would remain the same independent of the choice of scaling; normalising disturbances on a second quantity would establish a change in the disturbance receptivity that is counterbalanced by the difference in the two normalisations.

3.5. *Receptivity formula*

Stationary cross-flow disturbances $\boldsymbol{q} = (\boldsymbol{u}, p)$, excited by surface roughness, are assumed to be of the form (3.9) scaled by a receptivity amplitude A,

$$\boldsymbol{q}(r, \theta, z, t) = A\hat{\boldsymbol{q}}(r, z)\mathrm{e}^{\mathrm{i}n\theta}. \tag{3.14}$$

The size of the amplitude A is then dependent on the location and shape of the roughness. For the following study, we assume (for the purposes of simplifying the problem and analysis) that the roughness is periodic with respect to the azimuthal direction and modelled via a linearisation of the boundary condition (3.3*a*) for $\boldsymbol{u}$ as

$$u_{r,w} = -\frac{r}{Re}F'(0)h(r)\mathrm{e}^{\mathrm{i}n\theta}, \quad u_{\theta,w} = -\frac{r}{Re}G'(0)h(r)\mathrm{e}^{\mathrm{i}n\theta}, \quad u_{z,w} = 0 \quad \text{on } z = 0, \tag{3.15a–c}$$

where $h = h(r)$ represents the radial height of the surface roughness that is imposed on the finite radial interval $r_a \leqslant r \leqslant r_b$. (The w subscript in (3.15) references the disc wall.) Assuming $h = 0$ for all radii $r < r_a$ and $r > r_b$, then the receptivity amplitude A of a linear perturbation (3.14) is given as the change in the disturbance magnitude between the radial positions $r = r_a$ and $r = r_b$. Moreover, in the instance that $h = 0$ for all radii r (a smooth disc without any natural surface roughness), the amplitude $A = 0$ and the stationary cross-flow instability is not established.

A formula for the receptivity amplitude A is then derived by following the procedure outlined in § 3.3 for (3.11) and (3.12). On coupling (3.14) with the Lagrange identity (3.4) and the modified boundary condition (3.15), and then integrating across the wall-normal direction $z \in [0, \infty)$ and the finite radial interval $r \in [r_a, r_b]$, we obtain the following

https://doi.org/10.1017/jfm.2021.717 Published online by Cambridge University Press

formula for the receptivity amplitude

$$A = \int_{r_a}^{r_b} J_z(\boldsymbol{q}, \tilde{\boldsymbol{q}})|_{z=0}\ \mathrm{d}r, \tag{3.16a}$$

where

$$J_z(\boldsymbol{q}, \tilde{\boldsymbol{q}})|_{z=0} = \frac{1}{Re}\left(u_{r,w}\left.\frac{\partial \tilde{u}}{\partial z}\right|_{z=0} + u_{\theta,w}\left.\frac{\partial \tilde{v}}{\partial z}\right|_{z=0}\right). \tag{3.16b}$$

In general, the receptivity amplitude A is complex. However, in the subsequent analysis we will only quote the absolute value of A. Thus, receptivity amplitudes A can be determined using the shape of the surface roughness h and the normalised adjoint solutions $\tilde{\boldsymbol{q}}$ to the ALNS system of equations (3.6).

For a given azimuthal mode number n, the development and growth of the linear and adjoint perturbation fields are unchanged by the roughness shape h (only the amplitude of the linear disturbance changes). Thus, the adjoint method significantly reduces the time required to compute receptivity amplitudes A. Unlike the LNS approach, where the system of equations (3.2) are solved separately for each roughness realisation, the adjoint scheme only requires the LNS and ALNS systems to be solved once. On computing the normalised adjoint perturbation fields $\partial\tilde{u}/\partial z_{z=0}$ and $\partial\tilde{v}/\partial z_{z=0}$, receptivity amplitudes A can be computed instantaneously for many thousands of roughness realisations.

4. Velocity–vorticity formulation

Disturbance characteristics for both the LNS and ALNS systems of equations are numerically simulated using a velocity–vorticity formulation, based on the numerical scheme developed by Davies & Carpenter (2001). Both the linear and adjoint forms of the velocity–vorticity approach are fully equivalent to the LNS and ALNS systems of equations (3.2) and (3.6), respectively.

4.1. *Linear scheme*

Total velocity and vorticity fields are decomposed as

$$\boldsymbol{U} = \boldsymbol{U_B} + \boldsymbol{u}, \quad \boldsymbol{\Omega} = \boldsymbol{\Omega_B} + \boldsymbol{\omega}, \tag{4.1a,b}$$

where $\boldsymbol{U_B}$ and $\boldsymbol{\Omega_B} = \boldsymbol{\nabla} \wedge \boldsymbol{U_B}$ represent the undisturbed velocity and vorticity of the basic state (2.6), while the velocity and vorticity perturbation variables are defined as

$$\boldsymbol{u} = (u_r, u_\theta, u_z) \quad \text{and} \quad \boldsymbol{\omega} = (\omega_r, \omega_\theta, \omega_z). \tag{4.1c,d}$$

Perturbation fields are separated into primary $(\omega_r, \omega_\theta, u_z)$ and secondary variables $(u_r, u_\theta, \omega_z)$. The evolution of linearised disturbances is then determined using the following set of governing equations:

$$\frac{\partial \omega_r}{\partial t} + \frac{1}{r}\frac{\partial N_z}{\partial \theta} - \frac{\partial N_\theta}{\partial z} - \frac{2}{Re}\left(\omega_\theta + \frac{\partial u_z}{\partial r}\right) = \frac{1}{Re}\left(\left(\nabla^2 - \frac{1}{r^2}\right)\omega_r - \frac{2}{r^2}\frac{\partial \omega_\theta}{\partial \theta}\right), \tag{4.2a}$$

$$\frac{\partial \omega_\theta}{\partial t} + \frac{\partial N_r}{\partial z} - \frac{\partial N_z}{\partial r} + \frac{2}{Re}\left(\omega_r - \frac{1}{r}\frac{\partial u_z}{\partial \theta}\right) = \frac{1}{Re}\left(\left(\nabla^2 - \frac{1}{r^2}\right)\omega_\theta + \frac{2}{r^2}\frac{\partial \omega_r}{\partial \theta}\right), \tag{4.2b}$$

$$\nabla^2 u_z = \frac{1}{r}\left(\frac{\partial \omega_r}{\partial \theta} - \frac{\partial (r\omega_\theta)}{\partial r}\right). \tag{4.2c}$$

https://doi.org/10.1017/jfm.2021.717 Published online by Cambridge University Press

Here $\boldsymbol{N} = (N_r, N_\theta, N_z)$ is defined as

$$\boldsymbol{N} = \boldsymbol{\Omega_B} \times \boldsymbol{u} + \boldsymbol{\omega} \times \boldsymbol{U_B} \tag{4.3a}$$

and

$$N_r = \frac{1}{Re}\left(rF'u_z - 2Gu_\theta + H\omega_\theta - rG\omega_z\right), \tag{4.3b}$$

$$N_\theta = \frac{1}{Re}\left(2Gu_r + rG'u_z + rF\omega_z - H\omega_r\right), \tag{4.3c}$$

$$N_z = \frac{r}{Re}\left(G\omega_r - F\omega_\theta - F'u_r - G'u_\theta\right). \tag{4.3d}$$

Equations (4.2*a*) and (4.2*b*) are the radial and azimuthal components of the vorticity transport equation in cylindrical coordinates, while (4.2*c*) is the wall-normal component of the Poisson equation. Although the convective term $\boldsymbol{N}$ is dependent on both the primary and secondary variables, the latter set of perturbation fields can be eliminated as they can be defined explicitly in terms of the former set of fields using the definition for vorticity and the solenoidal condition,

$$u_r = -\int_z^\infty \left(\omega_\theta + \frac{\partial u_z}{\partial r}\right) \mathrm{d}z, \tag{4.4a}$$

$$u_\theta = \int_z^\infty \left(\omega_r - \frac{1}{r}\frac{\partial u_z}{\partial \theta}\right) \mathrm{d}z, \tag{4.4b}$$

$$\omega_z = \frac{1}{r}\int_z^\infty \left(\frac{\partial (r\omega_r)}{\partial r} + \frac{\partial \omega_\theta}{\partial \theta}\right) \mathrm{d}z. \tag{4.4c}$$

Substituting (3.15*a*) and (3.15*b*) into the definitions (4.4*a*) and (4.4*b*) for the secondary variables gives the following integral constraints for the primary variables ω_θ and ω_r:

$$\int_z^\infty \omega_\theta \,\mathrm{d}z = -u_{r,w} - \int_z^\infty \frac{\partial u_z}{\partial r} \,\mathrm{d}z, \tag{4.5a}$$

$$\int_z^\infty \omega_r \,\mathrm{d}z = u_{\theta,w} + \int_z^\infty \frac{1}{r}\frac{\partial u_z}{\partial \theta} \,\mathrm{d}z. \tag{4.5b}$$

Condition (3.15*c*) for u_z on the disc wall is unchanged, while all perturbations are assumed to asymptote towards zero in the far-field limit.

The pressure perturbation field p is not explicitly given in the velocity–vorticity formulation but is required in normalising perturbation fields (recall § 3.3). Integrating (3.2*c*) with respect to the wall-normal z-direction gives the following definition for pressure:

$$p = \int_0^\infty \left(\frac{\partial u_z}{\partial t} + \frac{rF}{Re}\frac{\partial u_z}{\partial r} + \frac{G}{Re}\frac{\partial u_z}{\partial \theta} + \frac{1}{Re}\frac{\partial (Hu_z)}{\partial z} + \frac{1}{rRe}\left(\frac{\partial (r\omega_\theta)}{\partial r} - \frac{\partial \omega_r}{\partial \theta}\right)\right) \mathrm{d}z. \tag{4.6}$$

Finally, as we are only interested in the development of stationary linear disturbances, velocity $\boldsymbol{u}$ and pressure p perturbation fields are again decomposed as (3.9), while the vorticity perturbation is given as

$$\boldsymbol{\omega}(r, \theta, z, t) = \hat{\boldsymbol{\omega}}(r, z)\mathrm{e}^{\mathrm{i}n\theta} \tag{4.7}$$

for an integer-valued azimuthal mode number n.

https://doi.org/10.1017/jfm.2021.717 Published online by Cambridge University Press

4.2. *Adjoint scheme*

Adjoint velocity and vorticity perturbation fields are defined as

$$\tilde{\boldsymbol{u}} = (\tilde{u}_r, \tilde{u}_\theta, \tilde{u}_z) \quad \text{and} \quad \tilde{\boldsymbol{\omega}} = (\tilde{\omega}_r, \tilde{\omega}_\theta, \tilde{\omega}_z). \tag{4.8a,b}$$

Similar to the linear scheme, adjoint perturbations are separated into primary $(\tilde{\omega}_r, \tilde{\omega}_\theta, \tilde{u}_z)$ and secondary variables $(\tilde{u}_r, \tilde{u}_\theta, \tilde{\omega}_z)$. The three adjoint primary variables are given as solutions of the following set of governing equations:

$$\frac{\partial \tilde{\omega}_r}{\partial t} + \frac{1}{r}\frac{\partial \tilde{N}_z}{\partial \theta} - \frac{\partial \tilde{N}_\theta}{\partial z} - \frac{2}{Re}\left(\tilde{\omega}_\theta + \frac{\partial \tilde{u}_z}{\partial r}\right) = -\frac{1}{Re}\left(\left(\nabla^2 - \frac{1}{r^2}\right)\tilde{\omega}_r - \frac{2}{r^2}\frac{\partial \tilde{\omega}_\theta}{\partial \theta}\right), \tag{4.9a}$$

$$\frac{\partial \tilde{\omega}_\theta}{\partial t} + \frac{\partial \tilde{N}_r}{\partial z} - \frac{\partial \tilde{N}_z}{\partial r} + \frac{2}{Re}\left(\tilde{\omega}_r - \frac{1}{r}\frac{\partial \tilde{u}_z}{\partial \theta}\right) = -\frac{1}{Re}\left(\left(\nabla^2 - \frac{1}{r^2}\right)\tilde{\omega}_\theta + \frac{2}{r^2}\frac{\partial \tilde{\omega}_r}{\partial \theta}\right), \tag{4.9b}$$

$$\nabla^2 \tilde{u}_z = \frac{1}{r}\left(\frac{\partial \tilde{\omega}_r}{\partial \theta} - \frac{\partial (r\tilde{\omega}_\theta)}{\partial r}\right). \tag{4.9c}$$

Here $\tilde{\boldsymbol{N}} = (\tilde{N}_r, \tilde{N}_\theta, \tilde{N}_z)$ is defined as

$$\tilde{N}_r = \frac{1}{Re}\left(H\tilde{\omega}_\theta - rG\tilde{\omega}_z - 2(F\tilde{u}_r + G\tilde{u}_\theta)\right), \tag{4.10a}$$

$$\tilde{N}_\theta = \frac{1}{Re}\left(rF\tilde{\omega}_z - H\tilde{\omega}_r + 2(G\tilde{u}_r - F\tilde{u}_\theta)\right), \tag{4.10b}$$

$$\tilde{N}_z = \frac{1}{Re}\left(rG\tilde{\omega}_r - rF\tilde{\omega}_\theta - 2(rF'\tilde{u}_r + rG'\tilde{u}_\theta + H'\tilde{u}_z)\right). \tag{4.10c}$$

Definitions for the three adjoint secondary variables are equivalent to those expressions given in (4.4) for the linear secondary variables, while integral constraints for $\tilde{\omega}_\theta$ and $\tilde{\omega}_r$ are analogous to those equations given in (4.5) for ω_θ and ω_r. Additionally, the boundary condition for $\tilde{u}_z$ on the disc surface is identical to that given in (3.15*c*) for u_z, while all adjoint perturbations are assumed to approach zero in the far-field limit.

The adjoint perturbation field $\tilde{p}$, that is again required to normalise disturbances (recall § 3.3), is computed by integrating (3.6*c*) with respect to z to give

$$\tilde{p} = \int_0^\infty \left(\frac{\partial \tilde{u}_z}{\partial t} + \frac{rF}{Re}\frac{\partial \tilde{u}_z}{\partial r} + \frac{G}{Re}\frac{\partial \tilde{u}_z}{\partial \theta} + \frac{H}{Re}\frac{\partial (\tilde{u}_z)}{\partial z} - \frac{1}{Re}(rF'\tilde{u}_r + rG'\tilde{u}_\theta + H'\tilde{u}_z) - \frac{1}{rRe}\left(\frac{\partial (r\tilde{\omega}_\theta)}{\partial r} - \frac{\partial \tilde{\omega}_r}{\partial \theta}\right)\right) \mathrm{d}z. \tag{4.11}$$

Finally, adjoint velocity $\tilde{\boldsymbol{u}}$ and pressure $\tilde{p}$ perturbation fields are again decomposed as (3.10), while the adjoint vorticity perturbation is given as

$$\tilde{\boldsymbol{\omega}}(r, \theta, z, t) = \tilde{\hat{\boldsymbol{\omega}}}(r, z)\mathrm{e}^{-\mathrm{i}n\theta}. \tag{4.12}$$

4.3. *Receptivity formula*

The receptivity formula (3.16), for computing the amplitude A of stationary cross-flow vortices excited by surface roughness, is recast to include the adjoint vorticity perturbation

https://doi.org/10.1017/jfm.2021.717 Published online by Cambridge University Press

field $\tilde{\boldsymbol{\omega}}$ as

$$A = \int_{r_a}^{r_b} J_z(\boldsymbol{q}, \tilde{\boldsymbol{q}})|_{z=0}\, \mathrm{d}r, \tag{4.13a}$$

for

$$J_z(\boldsymbol{q}, \tilde{\boldsymbol{q}})|_{z=0} = u_{r,w}\frac{\tilde{\omega}_{\theta,w}}{Re} - u_{\theta,w}\frac{\tilde{\omega}_{r,w}}{Re}, \tag{4.13b}$$

where the subscript w again refers to the disc wall.

4.4. *Numerical methods*

Both of the respective linear and adjoint velocity–vorticity formulations, (4.2) and (4.9), are discretised using the numerical scheme developed by Davies & Carpenter (2001). A fourth-order centred, compact finite difference method is implemented in the radial direction, whilst a Fourier expansion (given by (3.9) and (3.10)) is utilised in the azimuthal direction.

Along the wall-normal z-direction, disturbances are expanded using a Chebyshev spectral series of order M with the primary variables expanded in terms of odd Chebyshev polynomials following the pattern

$$f(r, \theta, z, t) = \left\{\sum_{m=1}^{M} f_m(r, t) T_{2m-1}(\zeta)\right\} \mathrm{e}^{\pm \mathrm{i}n\theta}, \tag{4.14a}$$

while the secondary variables are given in terms of even Chebyshev polynomials

$$g(r, \theta, z, t) = \left\{\tfrac{1}{2} g_0(r, t) + \sum_{m=1}^{M} g_m(r, t) T_{2m}(\zeta)\right\} \mathrm{e}^{\pm \mathrm{i}n\theta}. \tag{4.14b}$$

(Note the sign in the exponential term is positive and negative for the linear and adjoint formulations, respectively.) Here T_m is the mth Chebyshev polynomial, with points mapped from the semi-infinite physical domain $z \in [0, \infty)$ onto a finite computational interval $\zeta \in (0, 1]$ via the coordinate transformation

$$\zeta = \frac{l}{l + z}, \tag{4.15}$$

where l is a stretching factor. For the subsequent investigation, $l = 4$ was found to give an appropriate spread of points along the wall-normal direction.

For the linear scheme, null conditions are imposed on all perturbation fields at the inner radial boundary. In the subsequent study it was determined that this did not affect the evolution of disturbances, providing the inner radius was sufficiently small and removed from any source of disturbances, i.e. surface roughness. At the outer radius we follow the strategies outlined by Davies & Carpenter (2001). The computational domain is chosen to be sufficiently large to ensure the outer radial boundary is always kept an appropriate distance from those locations that are of interest, i.e. the radial region that stationary cross-flow instabilities emerge and develop. Secondly, we assume that disturbances are wavelike at the outer radius and impose the following condition on all primary perturbation fields:

$$\frac{\partial^2 f}{\partial r^2} = -\alpha^2 f. \tag{4.16}$$

Here α denotes a complex-valued radial wavenumber that is set equal to the corresponding eigenvalue determined from a local linear stability analysis. For the adjoint formulation,

https://doi.org/10.1017/jfm.2021.717 Published online by Cambridge University Press

the inner and outer radial boundary conditions are reversed, since the adjoint perturbation develops upstream. Finally, both linear and adjoint disturbances are numerically simulated using a time marching procedure based on a combination of a predictor–corrector scheme and semi-implicit methods.

5. Results

5.1. *Normalising perturbation fields*

Before undertaking a receptivity investigation of stationary cross-flow vortices excited by randomly distributed surface roughness, we first illustrate how linear and adjoint disturbances were numerically simulated and normalised. In the subsequent discussion we illustrate this process for the case corresponding to the azimuthal mode number $n = 32$. A finite computational domain was first established in the (r, z)-plane. Well-resolved numerical solutions were obtained for a radial grid $150 \leqslant r \leqslant 750$, with a radial step size of 0.5 units. The inner and outer boundaries of the radial domain were carefully chosen to ensure that the structure of the linear and adjoint disturbances was obtained in full. Additionally, the upstream radial boundary corresponds to the reference radius r_o. Finally, $M = 96$ Chebyshev points were used along the wall-normal z-direction, which was more than sufficient to accurately compute the development of both the linear and adjoint disturbances.

5.1.1. *Linear perturbation*

Stationary linear and adjoint perturbation fields were excited by a Gaussian shaped surface roughness

$$h(r) = \frac{1}{\sqrt{2\pi c^2}} \exp\left(\frac{-(r - r_f)^2}{2c^2}\right), \tag{5.1}$$

where r_f denotes the radial location of the roughness and c^2 the variance. (In the subsequent discussion $c = 2$.) The linear disturbance was established by fixing the roughness about $r_f = 200$. This particular radial location was chosen as it is sufficiently far upstream of the onset of the stationary cross-flow instability, which first becomes linearly unstable about $r_c \approx 323$ for $n = 32$. The roughness excites a stationary cross-flow vortex that develops radially outwards. After sufficient time has passed, the disturbance has convected across the entire radial domain and is unchanged by further increments in time. (Disturbance development was simulated for both shorter and longer radial domains and the results were unchanged.)

Figure 2 displays several characteristics associated with the linear disturbance established above. The maximum absolute value of the azimuthal velocity perturbation field, $\max_z |u_\theta|$, is plotted in figure 2(*a*) as a function of r, while figure 2(*b*) depicts the corresponding contours of u_θ scaled on $\max_z |u_\theta|$ in the (r, z)-plane. The scaling was implemented here to assist visualisation of the disturbance development, which would otherwise be impossible due to the rapid spatial growth associated with this form of instability. Red and blue colours in figure 2(*b*) depict positive and negative valued contour levels, respectively. The radial location of the roughness in figures 2(*a*) and 2(*b*) is made evident by the respective small peak and red contours located about the radius $r = 200$. Immediately downstream of the roughness the amplitude of the disturbance decreases. This behaviour is to be expected, as this particular cross-flow instability does not become linearly unstable until the critical radius $r_c \approx 323$. However, radially downstream of

https://doi.org/10.1017/jfm.2021.717 Published online by Cambridge University Press

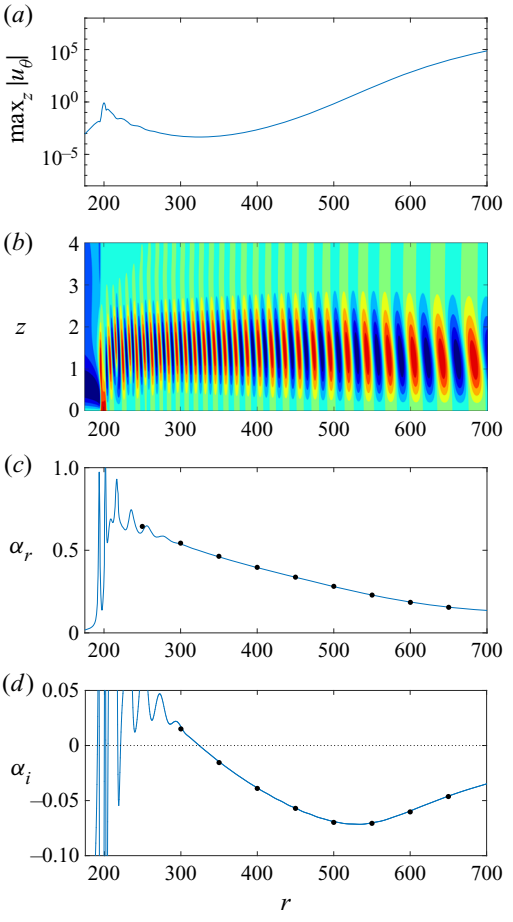


Figure 2. Characteristics of the linear azimuthal velocity perturbation field u_θ excited about $r_f = 200$, for an azimuthal mode number $n = 32$. (*a*) Plot of $\max_z |u_\theta|$ as a function of r. (*b*) Contours of $u_\theta / \max_z |u_\theta|$ in the (r, z)-plane. (*c*) Radial wavenumber α_r. (*d*) Radial growth rate α_i. The dot markers in (*c*,*d*) indicate those results obtained for fixed Reynolds numbers *Re* derived by applying the homogeneous flow approximation.

$r_c \approx 323$ the disturbance grows rapidly, and the cross-flow instability assumes the typical structure and develops near the disc surface.

The spatial development of the linear perturbation $\hat{\boldsymbol{q}}$ (recall (3.9)) may be decomposed as

$$\hat{\boldsymbol{q}}(r, z) = \check{\boldsymbol{q}}(r, z) \exp\left(\mathrm{i} \int_{r_c}^{r} \alpha(r')\, \mathrm{d}r'\right), \tag{5.2a}$$

where $\check{\boldsymbol{q}}$ is a slowly varying shape function and $\alpha = \alpha_r + \mathrm{i}\alpha_i$ represents the complex-valued radial wavenumber. The real and imaginary parts of α may be interpreted as the respective radial wavenumber and growth rate of the linear disturbance, and may be computed by considering the formula

$$\alpha = -\frac{\mathrm{i}}{f}\frac{\partial f}{\partial r}, \tag{5.2b}$$

where f is taken to be a measure of the disturbance amplitude at any given radial and wall-normal location. As before, the azimuthal velocity perturbation field u_θ was selected,

https://doi.org/10.1017/jfm.2021.717 Published online by Cambridge University Press

Re	α	$\tilde{\alpha}$
250	$0.644 + \mathrm{i}0.056$	$0.644 + \mathrm{i}0.070$
300	$0.532 + \mathrm{i}0.015$	$0.532 + \mathrm{i}0.008$
350	$0.464 - \mathrm{i}0.015$	$0.464 - \mathrm{i}0.022$
400	$0.397 - \mathrm{i}0.039$	$0.397 - \mathrm{i}0.045$
450	$0.337 - \mathrm{i}0.057$	$0.337 - \mathrm{i}0.062$
500	$0.282 - \mathrm{i}0.070$	$0.282 - \mathrm{i}0.073$
550	$0.229 - \mathrm{i}0.071$	$0.229 - \mathrm{i}0.074$
600	$0.185 - \mathrm{i}0.060$	$0.185 - \mathrm{i}0.065$
650	$0.155 - \mathrm{i}0.046$	$0.155 - \mathrm{i}0.050$

Table 1. Linear and adjoint radial wavenumbers, α and $\tilde{\alpha}$, for the azimuthal mode number $n = 32$, determined by applying the homogeneous flow approximation.

with computations based on measurements about the wall-normal height $z = 1.5$. (Note that the calculations for α were not noticeably affected by shifting the wall-normal z-location.)

The radial wavenumber α_r and growth rate α_i, associated with the above disturbance, are plotted in figures 2(c) and 2(d) and indicate that there is an initial transient phase before linearly unstable behaviour emerges about the critical radius $r_c \approx 323$. (Note that a negative valued α_i corresponds to radial growth and unstable behaviour.) The black dot markers in figures 2(c) and 2(d) depict the equivalent results obtained by solving the linear system of governing equations (4.2) with the homogeneous flow approximation, where the radial dependence of the undisturbed flow (2.6) is removed by fixing $r = Re$. To the accuracy of the illustration, the homogeneous flow computations about fixed radii are identical to the inhomogeneous flow solution, with results tabulated in table 1.

5.1.2. *Adjoint perturbation*

The corresponding adjoint perturbation field was generated by fixing the Gaussian shaped roughness (5.1) about the radius $r_f = 650$. Adjoint disturbances evolve in the spatially opposite sense to their linear counterparts and propagate upstream towards the inner radius. The dashed red line in figure 3(a) depicts the maximum absolute value of the adjoint perturbation field, $\max_z |\tilde{u}_\theta|$, while figure 3($b$) displays the contours of $\tilde{u}_\theta$ scaled on $\max_z |\tilde{u}_\theta|$. The adjoint disturbance grows radially inwards, attaining a peak amplitude near the radial location that the linear cross-flow instability first becomes unstable. Further upstream, the magnitude of $\max_z |\tilde{u}_\theta|$ decreases, which corresponds to a decay in the adjoint perturbation field.

Analogous to the linear perturbation, the spatial development of the adjoint perturbation $\tilde{\hat{\boldsymbol{q}}}$ (recall (3.10)) may be decomposed as

$$\tilde{\hat{\boldsymbol{q}}}(r, z) = \tilde{\check{\boldsymbol{q}}}(r, z) \exp\left(-\mathrm{i} \int_{\tilde{r}_c}^{r} \tilde{\alpha}(r')\, \mathrm{d}r'\right), \tag{5.3a}$$

where $\tilde{\check{\boldsymbol{q}}}$ is a slowly varying shape function and $\tilde{\alpha} = \tilde{\alpha}_r + \mathrm{i}\tilde{\alpha}_i$ represents the complex-valued adjoint radial wavenumber. (Note a change in sign has been imposed on the adjoint radial wavenumber as the adjoint disturbance grows radially inwards.) The adjoint radial wavenumber $\tilde{\alpha}$ is determined via the formula

$$\tilde{\alpha} = \frac{\mathrm{i}}{f} \frac{\partial f}{\partial r}, \tag{5.3b}$$

https://doi.org/10.1017/jfm.2021.717 Published online by Cambridge University Press

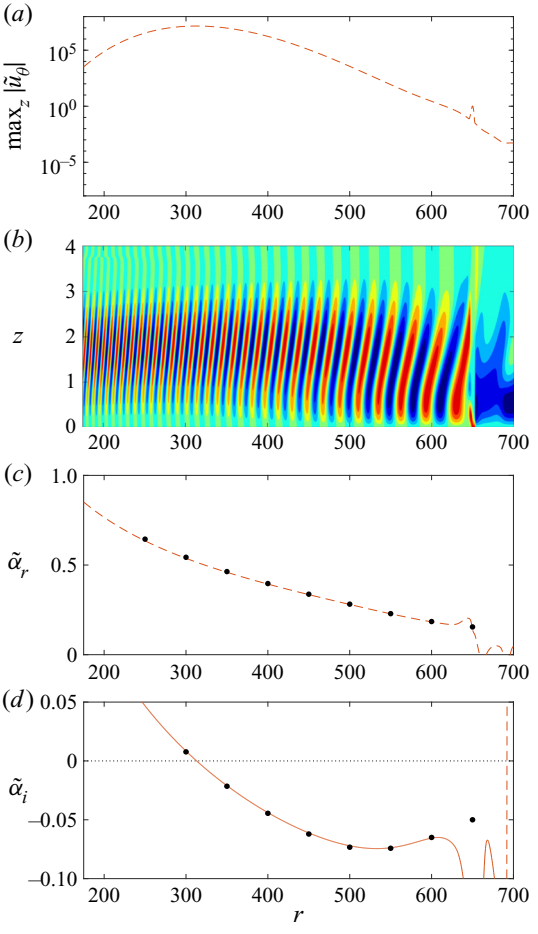


Figure 3. Characteristics of the adjoint azimuthal velocity perturbation field $\tilde{u}_\theta$ excited about $r_f = 650$, for an azimuthal mode number $n = 32$. (*a*) Plot of $\max_z |\tilde{u}_\theta|$ as a function of r. (*b*) Contours of $\tilde{u}_\theta / \max_z |\tilde{u}_\theta|$ in the (r, z)-plane. (*c*) Radial wavenumber $\tilde{\alpha}_r$. (*d*) Radial growth rate $\tilde{\alpha}_i$. The dot markers in (*c*,*d*) indicate those results obtained for fixed Reynolds numbers Re derived by applying the homogeneous flow approximation.

with f taken as the adjoint azimuthal velocity perturbation field $\tilde{u}_\theta$, measured about the wall-normal height $z = 1.5$.

Figures 3(*c*) and 3(*d*) depict the real and imaginary parts of $\tilde{\alpha}$, with the adjoint growth rate $\tilde{\alpha}_i = 0$ about the radius $\tilde{r}_c \approx 318$. (A negative valued $\tilde{\alpha}_i$ is matched to an adjoint perturbation growing radially inwards, while $\tilde{r}_c \neq r_c$ as a consequence of marginal differences between the linear and adjoint radial growth rates.) Black dot markers correspond to those solutions obtained by solving the equivalent adjoint system of governing equations (4.9) but with the application of the homogeneous flow approximation, i.e. the radius r is held fixed by setting it equal to the Reynolds number Re. Similar to the analysis of the linear perturbation, homogeneous flow calculations about fixed radii (tabulated in table 1) are indistinguishable from the inhomogeneous flow solutions. Moreover, the real parts of the linear and adjoint radial wavenumbers are identical: $\alpha_r = \tilde{\alpha}_r$. On the other hand, there are marginal differences in the corresponding imaginary parts: $\alpha_i \neq \tilde{\alpha}_i$. However, these small differences are counterbalanced by the normalisation (3.13).

https://doi.org/10.1017/jfm.2021.717 Published online by Cambridge University Press

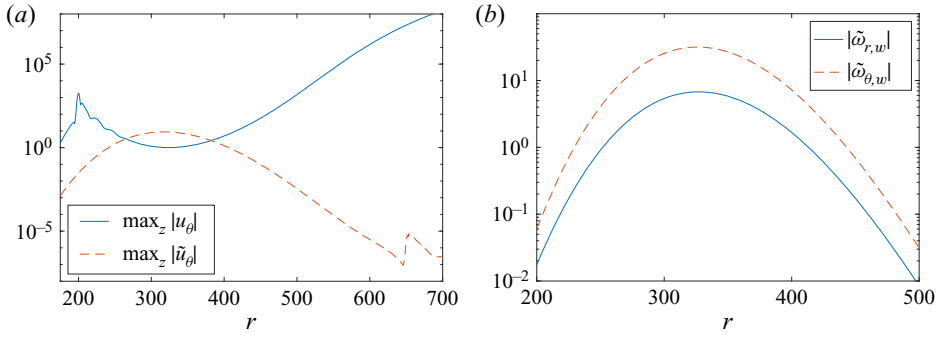


Figure 4. (*a*) Maximum absolute value of the linear and adjoint azimuthal velocity perturbation fields, $\max_z |u_\theta|$ and $\max_z |\tilde{u}_\theta|$, normalised using (3.13). (*b*) Corresponding normalised absolute value of the adjoint vorticity perturbation fields, $|\tilde{\omega}_{r,w}|$ and $|\tilde{\omega}_{\theta,w}|$. Solutions correspond to those parameter settings given in figures 2 and 3.

5.1.3. *Normalisation*

Linear and adjoint disturbances were then normalised using (3.13), with the corresponding azimuthal velocity perturbation fields, $\max_z |u_\theta|$ and $\max_z |\tilde{u}_\theta|$, plotted in figure 4(*a*). The line types and axes scales are the same as that given in figures 2(*a*) and 3(*a*), to help distinguish differences brought about by the normalisation. The linear solution is equal to unity about the radial location r_c for the onset of the stationary cross-flow instability, which is a requirement of the normalisation (3.13). On the other hand, the adjoint solution is scaled downwards and develops at a significantly smaller amplitude than before the normalisation.

Figure 4(*b*) displays the normalised absolute value of the adjoint vorticity perturbation fields $|\tilde{\omega}_{r,w}|$ (solid blue line) and $|\tilde{\omega}_{\theta,w}|$ (dashed red line) that are required to compute the receptivity amplitude A of the stationary cross-flow instability (recall (4.13)). The adjoint azimuthal vorticity perturbation field is almost an order of magnitude greater than the equivalent radial component. This would suggest that the azimuthal component of vorticity will have a greater influence on the receptivity of the rotating disc boundary layer to surface roughness. Furthermore, both adjoint perturbation fields achieve larger amplitudes about the radial location r_c associated with the onset of the linear disturbance. Thus, we might expect receptivity to be enhanced by roughness elements located within this particular radial region.

The above process was repeated for azimuthal mode numbers $n \in [25, 40]$ at unit step intervals. The decision to focus on this particular range of modes was made as a consequence of experimental investigations that typically observe cross-flow disturbances within this parameter range. Figure 5 depicts contours of $|\tilde{\omega}_{r,w}|$ and $|\tilde{\omega}_{\theta,w}|$ in the (r, n)-plane. For azimuthal mode numbers $n \leqslant 32$, the two adjoint vorticity components attain a peak over the radial range $250 \leqslant r \leqslant 350$. Beyond this annular region, both perturbation fields are significantly reduced. As n increases, the radial location that the two adjoint vorticity terms achieve a maxima is shifted radially downstream. This particular observation coincides with a corresponding radial shift downstream in the onset of the stationary cross-flow instability that occurs as n increases to larger values. Hence, for each azimuthal mode number n, receptivity will be most affected by surface roughness in the region that the stationary cross-flow instability first appears. This behaviour is consistent with that found in the flow over a swept wing. Radeztsky *et al.* (1999) undertook an experimental study on the flow over a swept wing with isolated roughness elements.

https://doi.org/10.1017/jfm.2021.717 Published online by Cambridge University Press

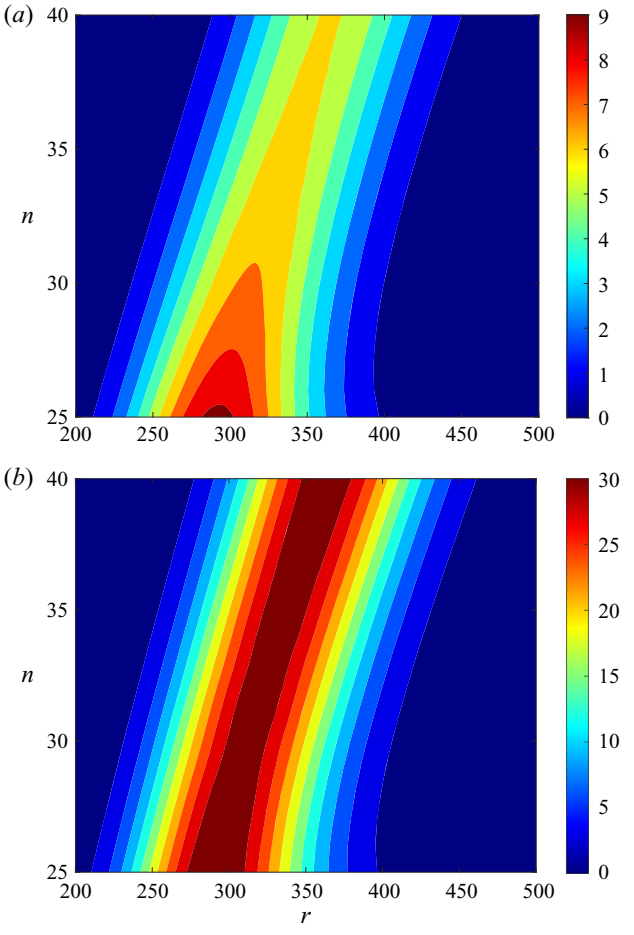


Figure 5. Contours in the (r, n)-plane of (*a*) $|\tilde{\omega}_{r,w}|$; (*b*) $|\tilde{\omega}_{\theta,w}|$.

Roughness centred about the location for neutral instability established the strongest receptivity, while roughness elements located further downstream had a negligible effect.

5.2. *Validation*

The adjoint scheme was validated by directly comparing adjoint predictions for the receptivity amplitude A against numerical solutions of the linear scheme (4.2). Linear disturbances were established by Gaussian shaped roughness elements (5.1) fixed about the radii $r_f = 300$, 325 and 350. The solid blue lines in figure 6 depict the maximum absolute value of the azimuthal velocity perturbation field, $\max_z |u_\theta|$, established by these three roughness distributions.

Coupling the receptivity formula (4.13) with the normalised adjoint vorticity perturbation fields $\tilde{\omega}_{r,w}$ and $\tilde{\omega}_{\theta,w}$, the amplitude A of the disturbance established by the three Gaussian shaped roughnesses was instantaneously computed as $A = 0.078$, 0.111 and 0.106, respectively. (Note that we only present the absolute value of the receptivity amplitude A here.) The dashed red lines in figure 6 illustrate the adjoint predictions for $\max_z |u_\theta|$ that were obtained by scaling the normalised linear perturbation field (plotted in figure 4*a*) by the above adjoint prediction for the amplitude A. In all three instances,

https://doi.org/10.1017/jfm.2021.717 Published online by Cambridge University Press

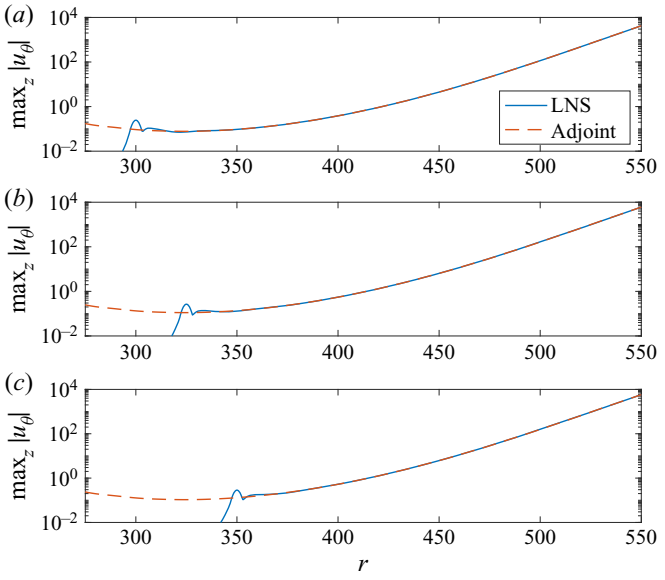


Figure 6. Maximum absolute value of the azimuthal velocity perturbation field, $\max_z |u_\theta|$, for the azimuthal mode number $n = 32$. Stationary cross-flow disturbance excited by a Gaussian shaped roughness centred about (*a*) $r_f = 300$; (*b*) $r_f = 325$; (*c*) $r_f = 350$. The LNS solution is given by the solid blue line, while the dashed red line depicts the adjoint prediction.

the linear and adjoint solutions are identical downstream of the roughness. Hence, the adjoint approach has correctly computed the amplitude A of the stationary cross-flow instability excited by the three Gaussian shaped roughness distributions. Several further test cases were modelled, for different roughness locations and shapes. In each instance, the adjoint method correctly predicted the amplitude of the equivalent LNS generated disturbance.

Having successfully tested the adjoint method for predicting the amplitude A of the disturbance established by simple Gaussian shaped roughness elements, we extend the investigation to realistic surface distributions. As the adjoint formula (4.13) only requires the adjoint perturbation fields $\tilde{\omega}_{r,w}$ and $\tilde{\omega}_{\theta,w}$ (given in figure 5) and the radial shape of the roughness $h(r)$ as inputs, the adjoint approach offers significant computational and time advantages over alternative receptivity strategies (i.e. LNS). Using (4.13), we undertake a rapid receptivity study of the rotating disc boundary layer to many thousands of randomly generated roughness realisations, of variable length and roughness settings.

5.3. *Randomly distributed surface roughness*

5.3.1. *Model*

Natural surface roughness is random and will be composed of several peaks and troughs of variable height, depth and wavelength. Mughal & Ashworth (2013) undertook a receptivity investigation of stationary cross-flow vortices on a swept wing, whereby three-dimensional roughness distributions were modelled using a Fourier cosine series. A simplification was made in the subsequent adjoint based study by Thomas *et al.* (2017), who assumed the roughness distribution was periodic along the spanwise direction. A similar simplification was implemented here, where due to the natural periodicity of the disc, surface roughness was assumed to be periodic in the azimuthal direction. Two-dimensional roughness

https://doi.org/10.1017/jfm.2021.717 Published online by Cambridge University Press

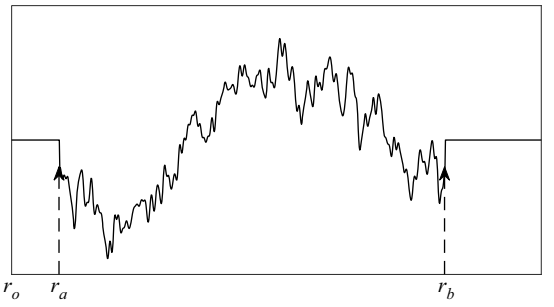


Figure 7. Diagram of the roughness model.

distributions were modelled as

$$h(r) = \sum_{j=N_{min}}^{N_{max}} a_j \cos\left(2\pi\left(\frac{jr}{r_\lambda} + \phi_j\right)\right), \tag{5.4}$$

where N_{min} and N_{max} specify long and short scale wavelength filters, and r_λ denotes a radial wavelength. Parameters a_j and ϕ_j represent randomly generated roughness amplitudes and phase shifts, respectively. Roughness distributions were then implemented on the radial interval $r_a \leqslant r \leqslant r_b$, where r_a and r_b specify the upstream and downstream boundaries of the surface roughness, respectively. Figure 7 displays a diagram of the roughness arrangement, including labels for the radial positions r_o, r_a and r_b. (Note that in the subsequent analysis, the downstream boundary of the roughness distribution $r_b \leqslant r_\lambda + r_a$.)

Each randomly generated amplitude a_j was then scaled by the factor

$$\left(\frac{r_\lambda}{2\pi j}\right)^k \tag{5.5}$$

for a power law coefficient k. An identical modelling approach was implemented by Raposo *et al.* (2018) in their acoustic receptivity study of TS waves in the presence of surface roughness. This particular model for roughness was utilised here as it is well known that the power spectral density (PSD) for natural surface roughness follows a power law of the form (5.5) (Van Deusen 1967; Sayles & Thomas 1978; Jacobs, Junge & Pastewka 2017). For instance, it was shown by Mughal & Ashworth (2013) that the energy in the PSD of a painted panel or unpainted aluminium plate was primarily found in the longer wavelengths. Furthermore, Van Deusen (1967) noted that the PSD decreased with the square of the angular frequency for many natural and artificial surfaces, while Raposo *et al.* (2018) set the coefficient $k = 1$ in their receptivity investigation to ensure the PSD decayed at the rate found by Van Deusen.

Finally, all roughness distributions were scaled on the r.m.s., which is defined as

$$h_{rms} = \sqrt{\frac{1}{r_b - r_a}\int_{r_a}^{r_b} h^2 \,\mathrm{d}r}. \tag{5.6}$$

For instance, setting $h_{rms} = 10^{-3}$ corresponds to a surface roughness with a r.m.s. equal to 0.1 % of the boundary layer thickness δ.

Figure 8 depicts several randomly generated roughness distributions (solid blue lines), along with their respective gradients $\mathrm{d}h/\mathrm{d}r$ (dashed red) in the instance the roughness

https://doi.org/10.1017/jfm.2021.717 Published online by Cambridge University Press

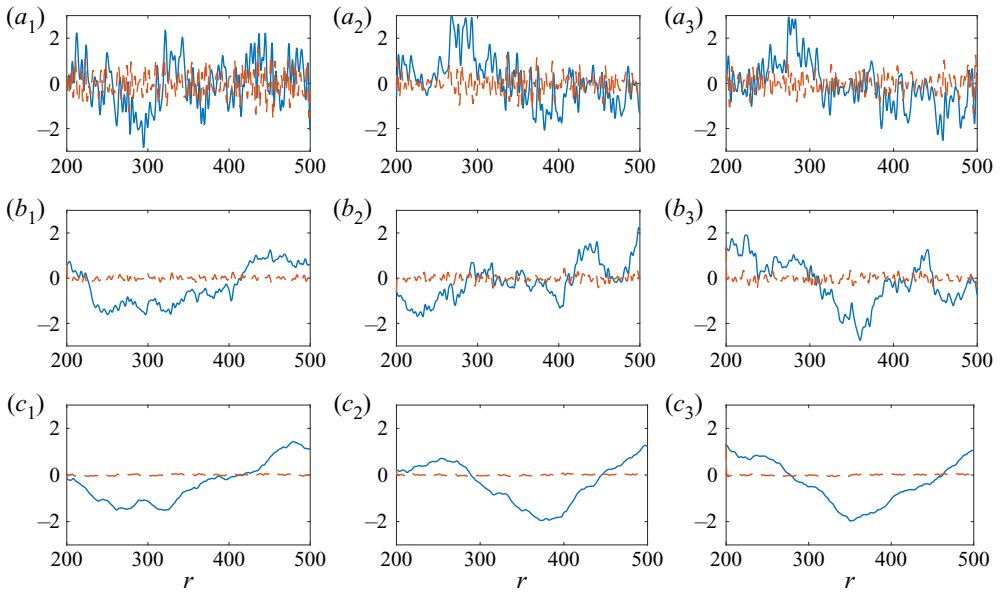


Figure 8. Examples of surface roughness for $N_{min} = 1$, $N_{max} = 100$, $h_{rms} = 1$ and $(a_\star)$ $k = 0.5$; $(b_\star)$ $k = 1$; $(c_\star)$ $k = 1.5$. The solid blue and dashed red lines depict roughness distributions h and their corresponding gradients $\mathrm{d}h/\mathrm{d}r$.

parameter $h_{rms} = 1$. The long and short scale wavelength filters are set to the respective values $N_{min} = 1$ and $N_{max} = 100$, while each roughness is fixed about the radial interval $200 \leqslant r \leqslant 600$ and $r_\lambda = 400$. The power law coefficient k increases from $k = 0.5$ in figure 8(a) to $k = 1.5$ in figure 8(c), at 0.5 step intervals. The illustration clearly shows that each roughness realisation is distinct and encompasses a variety of wavelengths. Furthermore, the effect of the power law coefficient k on the form of the roughness is demonstrated. For small k, shorter wavelengths are significant that establish many peaks and troughs with relatively large gradients. However, as the coefficient k increases, shorter wavelengths have a limited influence on the structure of the roughness, resulting in fewer sharp variations and significantly smaller gradients.

Averaging over many thousands of roughness realisations, it was determined that the mean of the absolute value of the surface gradient, $|\mathrm{d}h/\mathrm{d}r|$, was approximately 0.4 when $k = 0.5$, but reduces as k increases; $|\mathrm{d}h/\mathrm{d}r| \approx 0.1$ and 0.05 for $k = 1$ and $k = 1.5$, respectively. These trends are then scaled linearly with the r.m.s. of the roughness. In the subsequent analysis we assume that any significant spikes or troughs in the surface roughness are not sufficient to bring about boundary layer separation or the nonlinear stages of laminar–turbulent transition.

An additional roughness realisation is plotted in figure 9(a) that is established using those parameter settings given in figure 8(b). The response of the azimuthal velocity perturbation field u_θ, to this particular roughness, is then shown in figure 9(b,c). The maximum absolute value of the azimuthal velocity perturbation field, $\max_z |u_\theta|$, determined via the LNS formulation (4.2) is given by the solid blue line in figure 9(b), while the equivalent adjoint prediction is given by the dashed red line. (Recall that the adjoint formula (4.13) only requires the normalised adjoint vorticity fields $\omega_{r,w}$ and $\omega_{\theta,w}$, and the roughness shape h, as inputs.) The amplitude A of the disturbance established by the given roughness was determined using the adjoint formula (4.13) as $A = 0.29$.

https://doi.org/10.1017/jfm.2021.717 Published online by Cambridge University Press

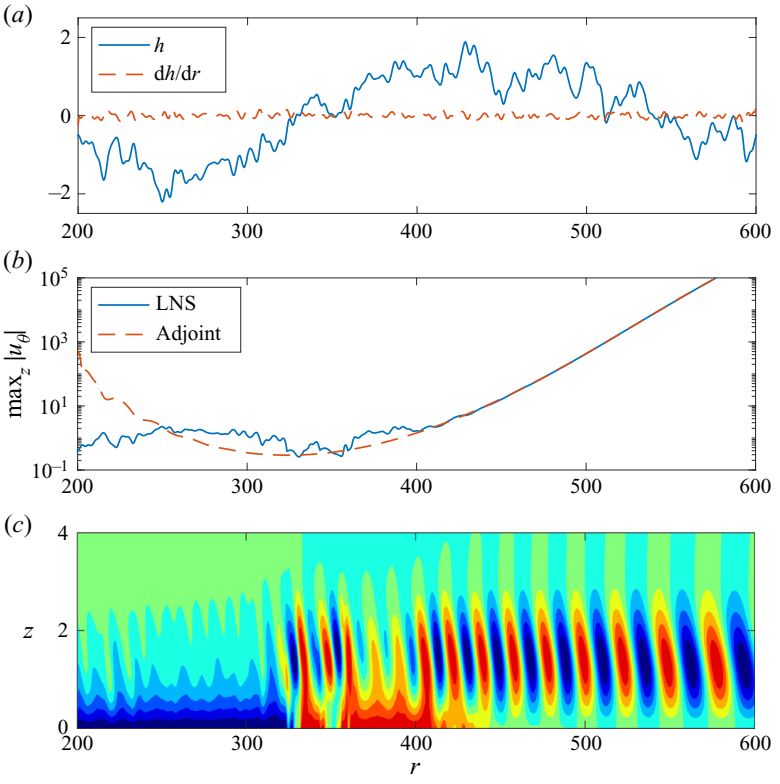


Figure 9. (*a*) Randomly generated roughness distribution h and gradient $\mathrm{d}h/\mathrm{d}r$. (*b*) Maximum absolute value of the azimuthal velocity perturbation field, $\max_z |u_\theta|$. The LNS solution is given by the solid blue line, while the dashed red line depicts the adjoint prediction. (*c*) Contours of u_θ, scaled on $\max_z |u_\theta|$, in the (r, z)-plane.

As with the simpler Gaussian shaped roughness distributions, the LNS solution and adjoint prediction are indistinguishable. Thus, the adjoint approach has again correctly determined the amplitude A of the disturbance.

The depiction of $\max_z |u_\theta|$ in figure 9(*b*) and the contours of u_θ in figure 9(*c*) indicate that the disturbance achieves magnitudes greater than the height of the roughness about the radius $r = 400$. Beyond this radial location the disturbance grows rapidly, and the response of the linear perturbation is not affected by roughness elements located further outboard. Hence, receptivity is greatest in the radial region that the stationary cross-flow instability first becomes linearly unstable.

5.3.2. *Mean receptivity*

For the remainder of this investigation, the long wavelength filter $N_{min} = 1$ and the wavelength parameter $r_\lambda = 400$. Additionally, the upstream boundary of the roughness distribution was fixed about $r_a = 200$, which is sufficiently far upstream of the radial region that receptivity is expected to be the most significant. The downstream boundary r_b of the roughness distribution and the short wavelength filter N_{max} were then varied to determine the effects, if any, on the receptivity process. Additionally, several values of the power law coefficient k were modelled.

https://doi.org/10.1017/jfm.2021.717 Published online by Cambridge University Press

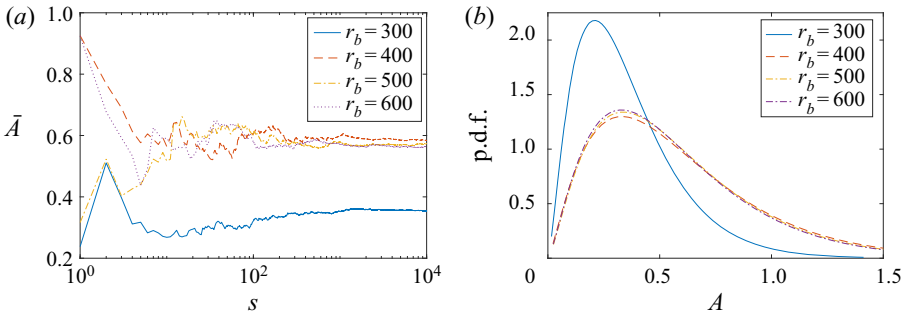


Figure 10. (*a*) Mean amplitude $\bar{A}$ against the number of roughness realisations s. (*b*) Probability density functions. The azimuthal mode number $n = 32$ and roughness parameters $N_{max} = 100$, $h_{rms} = 1$, $k = 1$ and variable r_b.

There are two major objectives of the following analysis.

(i) Determine those roughness characteristics that are most significant in the receptivity process, and establish the largest disturbance amplitudes A.
(ii) For a disc with a known roughness r.m.s., compute the mean disturbance amplitudes and determine the radial region that disturbances achieve sufficiently large magnitudes to invalidate the linear stability assumptions. Moreover, these calculations will be used as initial inputs in a future fully nonlinear stability study.

A Monte-Carlo uncertainty quantification analysis was undertaken, whereby several thousand roughness distributions were randomly generated and receptivity amplitudes A computed. Mean amplitudes $\bar{A}$ were then determined via the formula

$$\bar{A} = \sum_{s} A/s, \tag{5.7}$$

for s roughness realisations. (Calculations were again based on the absolute value of A.) Figure 10(*a*) displays mean amplitudes $\bar{A}$ as a function of the number of roughness realisations s, for four downstream boundaries r_b. The azimuthal mode number $n = 32$ and the low wavelength filter $N_{max} = 100$, while the roughness parameter h_{rms} and power law coefficient k were both set to unity. A log scaling is used along the horizontal s-axis to illustrate the variation in $\bar{A}$ as s increases. In all instances modelled, the size of $\bar{A}$ converges towards a fixed constant after approximately 1000 roughness iterations. Further iterations were not found to bring about any significant changes in the mean amplitude. Although a different mean amplitude was realised for each r_b considered, results indicate that variations in $\bar{A}$ diminish as r_b increases. Thus, surface roughness located sufficiently far outboard has a negligible effect on the mean amplitude of the stationary cross-flow instability.

Probability density functions (p.d.f.s) are plotted in figure 10(*b*), which were generated using the routines available in MATLAB. Each p.d.f. was constructed using $s = 10^4$ roughness realisations and the absolute value of the receptivity amplitude A. Solutions indicate that a greater variance in the amplitude A is achieved as the length of the roughness distribution increases. Moreover, the illustration shows that receptivity can vary significantly from one realisation to the next. It is hypothesised that the larger amplitudes are associated with roughness distributions that encompass significant isolated peaks (and troughs) in the radial region that receptivity is most enhanced, i.e. where the cross-flow vortex first becomes linearly unstable.

https://doi.org/10.1017/jfm.2021.717 Published online by Cambridge University Press

Mean amplitudes $\bar{A}$ are plotted as a function of the low wavelength filter N_{max} (for $r_b = 600$) in figure 11(*a*) and the downstream boundary r_b of the roughness (for $N_{max} = 100$) in figure 11(*b*). Solutions again correspond to the stationary cross-flow instability established for the azimuthal mode number $n = 32$, while roughness parameters $h_{rms} = 1$ and $k \in [0.5, 1.5]$. Moreover, computations are based on $s = 10^4$ roughness realisations, which was more than sufficient for $\bar{A}$ to achieve a converged state in all cases modelled. The size of the mean amplitude $\bar{A}$ increases sharply in figure 11(*a*) when N_{max} exceeds 20. This particular observation coincides with the shortest roughness scale matching the wavelength of the cross-flow instability. The radial wavenumber α_r of the stationary cross-flow instability is within the range $0.25 \leqslant \alpha_r \leqslant 0.5$ (recall figure 2*c*), while the wavenumber associated with the shortest roughness scale in (5.4) is given as $2\pi N_{max}/r_\lambda \approx 0.31$ for $N_{max} = 20$. Similar observations were observed by Thomas *et al.* (2017) in their receptivity study of cross-flow vortices over a swept wing. With the exception of the case $k = 0.5$ (solid blue line), mean amplitudes $\bar{A}$ approach a fixed constant for $N_{max} \approx 40$, which corresponds to a roughness length scale that is approximately half of the wavelength of the cross-flow instability. Hence, shorter roughness scales have a negligible effect on the receptivity process, which is to be expected given the power law scale factor (5.5). In the instance the power law coefficient $k = 0.5$, $\bar{A}$ is observed to decrease for $N_{max} > 40$. However, if results were extended to larger valued N_{max}, than that plotted in figure 11(*a*), results would eventually converge towards a fixed value as the shorter roughness scales would become insignificant. Finally, as k increases, the size of the mean amplitude $\bar{A}$ decreases. Indeed, there is an order of magnitude difference in $\bar{A}$ between the smallest and largest valued k modelled. The significance of the short roughness scales of commensurate size to the wavelength of the cross-flow instability, diminish for larger valued k.

Results plotted in figure 11(*b*) indicate that the mean amplitude $\bar{A}$ increases rapidly for radii $r_b > 250$, and in most instances asymptotes towards a fixed constant for $r_b > 400$. (There is a noticeable exception for cases $k > 1$, where $\bar{A}$ attains a maximum value near $r_b \approx 330$ and then decreases towards a fixed constant for larger valued r_b. This behaviour can again be attributed to the diminished effect of the short roughness scales that occurs for larger valued k.) These observations are consistent with our earlier predictions that receptivity is most affected by roughness distributions located about the radial region that the disturbance first becomes linearly unstable and where the adjoint vorticity terms were most significant (recall figures 4(*b*) and 5).

The above analysis was extended to azimuthal mode numbers $n \in [25, 40]$, for roughness parameter settings $N_{max} = 100$, $r_b = 600$ and $h_{rms} = 1$. These particular settings were chosen as receptivity calculations were unchanged by further increases in the short wavelength filter N_{max} or the downstream boundary r_b of the roughness. Figure 12 displays the mean amplitude $\bar{A}$ and corresponding standard deviations σ as functions of n, for five values of the power law coefficient k. Calculations are again based on $s = 10^4$ roughness realisations. For each k considered, the standard deviation σ is approximately half of the corresponding mean amplitude $\bar{A}$. Thus, there is a significant variation in the initial amplitude of the stationary cross-flow instability. Additionally, there is a small increase in $\bar{A}$ as the azimuthal mode number n increases. However, this does not necessarily imply that these larger valued n modes will play a greater role in the laminar–turbulent transition process, as smaller valued n modes become unstable earlier. The cross-flow mode that is ultimately responsible for bringing about the latter stages of convective driven transition is governed by the amplitude A, the radial growth rate α_i and the size of the roughness that is characterised in this investigation by the parameter h_{rms}.

https://doi.org/10.1017/jfm.2021.717 Published online by Cambridge University Press

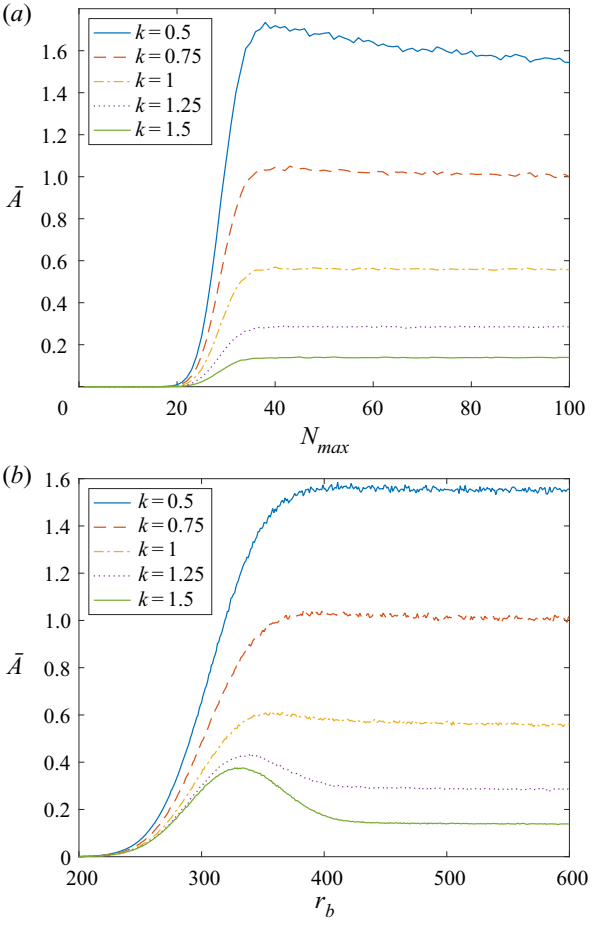


Figure 11. Mean amplitude $\bar{A}$ as a function of (*a*) N_{max} for $r_b = 600$ and (*b*) r_b for $N_{max} = 100$. Computations are based on $s = 10^4$ roughness iterations for $n = 32$, and roughness parameters $h_{rms} = 1$ and variable k.

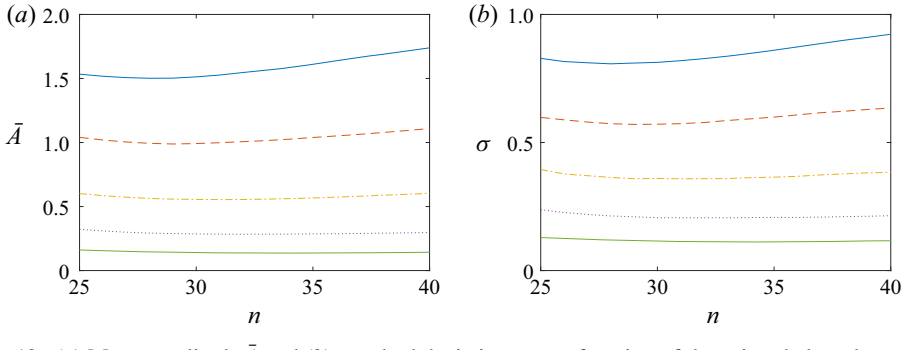


Figure 12. (*a*) Mean amplitude $\bar{A}$ and (*b*) standard deviation σ as a function of the azimuthal mode number n and variable k. Computations are based on $s = 10^4$ roughness iterations, and roughness parameters $h_{rms} = 1$, $N_{max} = 100$ and $r_b = 600$. Line types are the same as those given in figure 11.

https://doi.org/10.1017/jfm.2021.717 Published online by Cambridge University Press

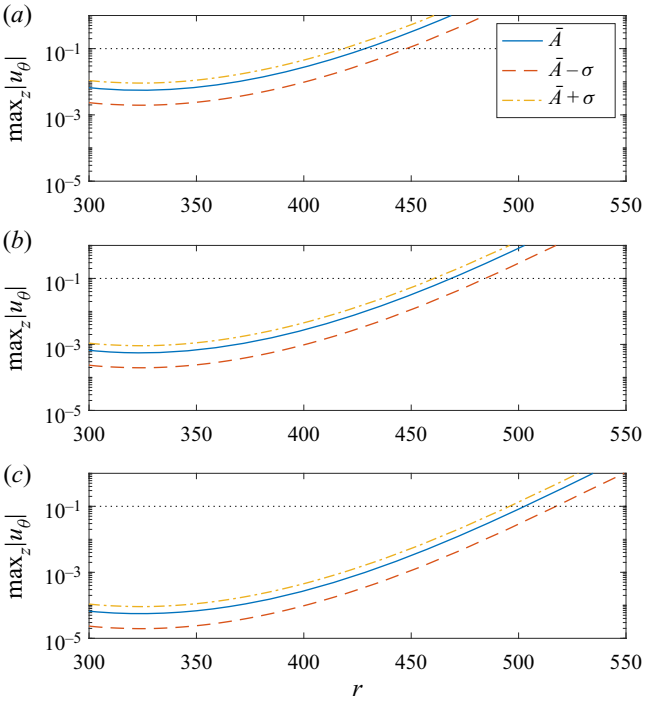


Figure 13. Maximum absolute value of the azimuthal velocity perturbation field, $\max_z |u_\theta|$, as a function of the radius r for $n = 32$ and (*a*) $h_{rms} = 10^{-2}$; (*b*) $h_{rms} = 10^{-3}$; (*c*) $h_{rms} = 10^{-4}$. Calculations are based on those roughness parameters given in figure 12 when $k = 1$. The horizontal dotted line corresponds to $\max_z |u_\theta| = 10^{-1}$.

5.3.3. *Predicting the onset of nonlinear behaviour and other processes*

Mean amplitudes $\bar{A}$ are coupled to the radial growth of the normalised azimuthal velocity perturbation field u_θ (as plotted in figure 4(*a*) for $n = 32$) to predict the radial location that we might expect the linear stability assumptions to no longer be appropriate, and where nonlinear effects and other transition processes to have emerged. Since the analysis is linear, scaling the surface roughness on the parameter h_{rms} equates to an equivalent scaling on the disturbance amplitude. Thus, fixing $h_{rms} = 10^{-3}$ corresponds to setting the mean amplitude of the disturbance to $10^{-3}\bar{A}$, with $\bar{A}$ as given in figure 12. Furthermore, we assume that the linear stability assumptions are no longer appropriate once $\max_z |u_\theta| = 10^{-1}$. This particular assumption was based on earlier observations within the literature. For instance, Balachandar, Streett & Malik (1992) reported that the primary instability has to attain a threshold value of 9 % of the undisturbed flow (2.6) in order for secondary instabilities to grow. Hence, $r_{u_\theta=0.1}$ denotes the radial location used here to distinguish between the linear and nonlinear stages of convectively forced laminar–turbulent transition. (In experiments, the threshold between linear and nonlinear effects may arise at smaller disturbance amplitudes than that implemented here. Moreover, travelling waves, the absolutely unstable mechanism or secondary instabilities may develop, and establish nonlinear behaviour and the onset of laminar–turbulent transition at earlier radii than that presented in the subsequent analysis. Thus, the radial location $r_{u_\theta=0.1}$ should only be viewed as an upper bound for when we might expect disturbance development to be no longer governed by linear stability theory.)

Figure 13 displays the maximum absolute value of the azimuthal velocity perturbation field, $\max_z |u_\theta|$, as a function of the radius r for the azimuthal mode number $n = 32$.

https://doi.org/10.1017/jfm.2021.717 Published online by Cambridge University Press

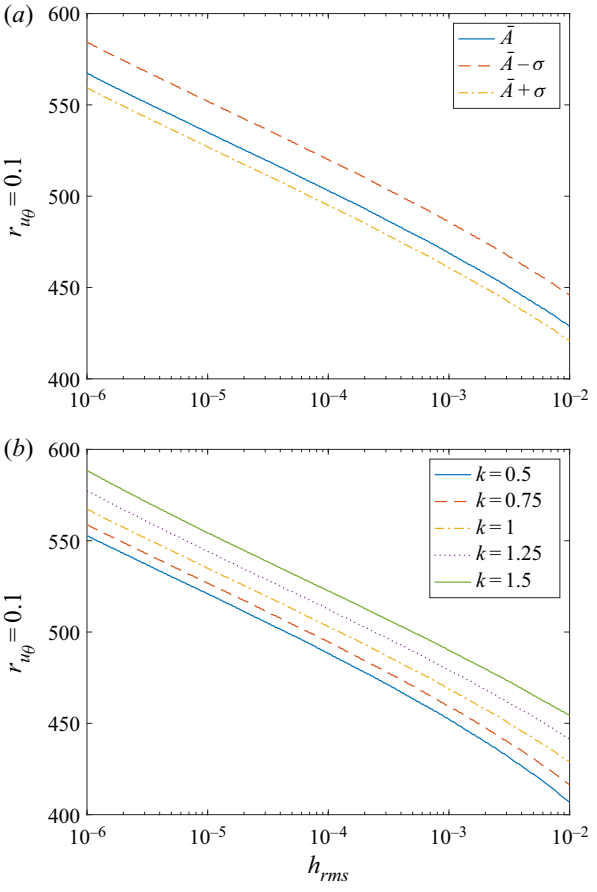


Figure 14. The radius r that the maximum absolute value of the azimuthal velocity perturbation field, $\max_z |u_\theta| = 10^{-1}$, for $n = 32$ and those roughness parameters given in figure 12. (*a*) Calculations are based on the mean amplitude $\bar{A}$ and standard deviation σ for $k = 1$. (*b*) Calculations are based on $\bar{A}$ and variable k.

Solution curves were obtained by scaling the normalised solution depicted in figure 4(*a*), by the adjoint predictions for the mean amplitude $\bar{A}$ presented in figure 12, with k set to unity. The horizontal dotted line indicates when $\max_z |u_\theta| = 10^{-1}$. (Computations based on other k values brought about a small change in the radial interval that $\max_z |u_\theta| = 10^{-1}$ was realised.) The r.m.s. of the roughness decreases by an order of ten monotonically down figure 13, with $h_{rms} = 10^{-2}$ and 10^{-4} in figures 13(*a*) and 13(*c*), respectively. Solid blue line-types depict results based on the mean amplitude $\bar{A}$, while the remaining two line-types give an indication of the spread of solutions, with the disturbance amplitude set to $\bar{A} \pm \sigma$. Results indicate that $\max_z |u_\theta| = 10^{-1}$ is realised about the successive radial intervals $r \in [418, 450]$, $[460, 485]$ and $[495, 520]$, for the three respective h_{rms} values modelled. This was extended to $r \in [528, 550]$ and $[560, 583]$ for $h_{rms} = 10^{-5}$ and 10^{-6}, respectively. Hence, for a fixed h_{rms}, there is a short annular region in which we might expect the stationary cross-flow vortex, established by surface roughness, to achieve amplitudes sufficient to invalidate the linear stability assumptions and bring about nonlinear effects. Furthermore, results clearly demonstrate that a smooth disc will delay the onset of convective induced transition to larger radii, which may allow the absolutely unstable mechanism to develop and play a role in the laminar–turbulent transition process.

https://doi.org/10.1017/jfm.2021.717 Published online by Cambridge University Press

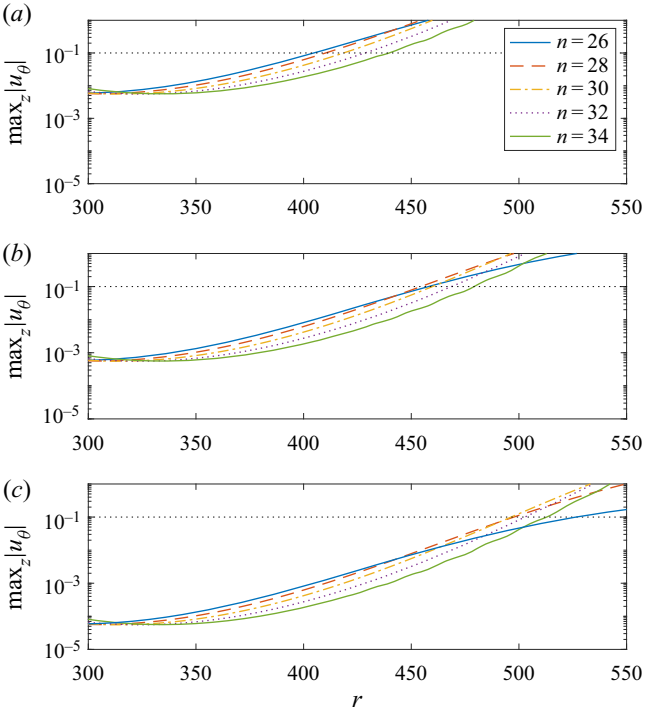


Figure 15. Maximum absolute value of the azimuthal velocity perturbation field, $\max_z |u_\theta|$, as a function of the radius r for variable azimuthal mode numbers n and (*a*) $h_{rms} = 10^{-2}$; (*b*) $h_{rms} = 10^{-3}$; (*c*) $h_{rms} = 10^{-4}$. Mean amplitudes $\bar{A}$ are based on those roughness parameter settings given in figure 12 when $k = 1$. The horizontal dotted line corresponds to $\max_z |u_\theta| = 10^{-1}$.

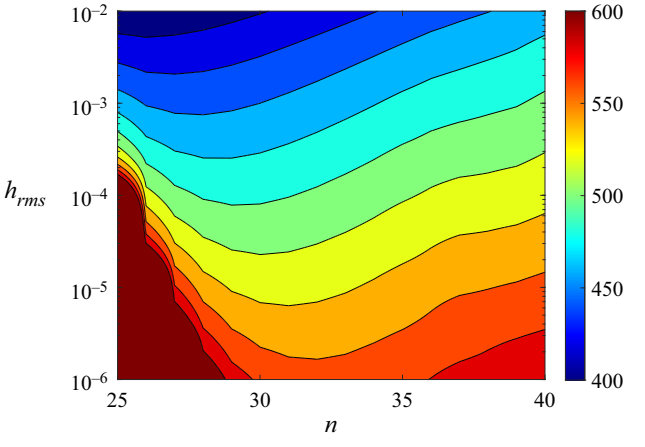


Figure 16. Contours of the radius $r_{u_\theta=0.1}$ in the (n, h_{rms})-plane that the maximum absolute value of the azimuthal velocity perturbation field, $\max_z |u_\theta| = 10^{-1}$. Mean amplitudes $\bar{A}$ are based on those roughness parameter settings given in figure 12 when $k = 1$.

The radial location $r_{u_\theta=0.1}$ is plotted in figure 14 as a function of h_{rms}. Calculations are again based on the adjoint predictions presented in figure 12 for $n = 32$. The first illustration, figure 14(*a*), gives an indication of the spread of $r_{u_\theta=0.1}$ for the case where the

https://doi.org/10.1017/jfm.2021.717 Published online by Cambridge University Press

power law coefficient $k = 1$. The second plot, figure 14(b), depicts the effect of varying the power law coefficient k. As expected, results show that the radial location $r_{u_\theta=0.1}$ emerges further downstream as h_{rms} decreases. Furthermore, for $h_{rms} \leqslant 10^{-2}$, the radius $r_{u_\theta=0.1}$ is approximated by the formula

$$r_{u_\theta=0.1} = c - d \log_{10} h_{rms} \tag{5.8}$$

for positive valued constants c and d that are dependent on k. (Similar depictions of $r_{u_\theta=0.1}$ were realised for other stationary cross-flow disturbances with different azimuthal mode numbers.) Assuming that experimental roughness characteristics are known and that the $n = 32$ cross-flow mode is responsible for bringing about convective driven transition, figure 14 and this particular logarithmic relationship may be used to predict the radial range when transition in the rotating disc boundary layer is likely to occur, or at least when nonlinear effects and other processes must be accounted for. Finally, results imply that $r_{u_\theta=0.1}$ occurs further downstream for larger valued k, which is to be expected given our earlier observations: mean amplitudes $\bar{A}$ decrease as k increases.

The maximum absolute value of the azimuthal velocity perturbation field, $\max_z |u_\theta|$, is plotted in figure 15 for several azimuthal mode numbers n. Computations are again based on the mean calculations presented in figure 12 for $k = 1$, while the roughness parameter h_{rms} is as indicated in the caption. The horizontal dotted line again specifies when $\max_z |u_\theta| = 10^{-1}$. Solutions plotted in figure 15(a) indicate that the $n = 26$ cross-flow mode (solid blue line) attains this threshold value about $r \approx 400$ when $h_{rms} = 10^{-2}$, which is radially inboard of the locations that the other modes achieve this particular amplitude. Thus, the $n = 26$ mode will be responsible for engineering the early stages of transition in this instance. As h_{rms} decreases, the stationary cross-flow mode n that first achieves the amplitude $\max_z |u_\theta| = 10^{-1}$, increases. For $h_{rms} = 10^{-3}$ and 10^{-4}, cross-flow modes $n = 28$ (dashed red) and 30 (chain yellow) are the first to attain the linear-nonlinear threshold amplitude about the respective radial positions $r \approx 450$ and 500.

Contours of the radius $r_{u_\theta=0.1}$ are plotted in figure 16 in the (n, h_{rms})-plane, for those roughness settings given in figure 12 and $k = 1$. Blue contour levels correspond to radii $r \sim 400$, while red contours are matched to $r \sim 600$. The illustration further supports our above comments that azimuthal mode numbers on the interval $25 \leqslant n \leqslant 30$ will most likely bring about nonlinear effects when the roughness parameter $h_{rms} \geqslant 10^{-4}$. However, for smaller valued h_{rms}, larger valued azimuthal mode numbers (such as $n = 32$) grow at a faster rate and attain amplitudes $\max_z |u_\theta| = 10^{-1}$ earlier. Hence, these particular stationary cross-flow instabilities will play a greater role in the early stages of laminar–turbulent transition on a clean rotating disc.

6. Conclusions

The receptivity of the rotating disc boundary layer to surface roughness was investigated using adjoint methods. The ALNS equations in cylindrical coordinates were derived and receptivity characteristics were computed using a fully equivalent velocity–vorticity formulation (that is based on the numerical scheme developed by Davies & Carpenter 2001). Stationary cross-flow vortices were excited by surface roughness that was modelled using a two-dimensional Fourier cosine series (5.4) and implemented via a linearisation of the no-slip condition. Each roughness distribution was scaled on its respective r.m.s. and composed of many roughness length scales (both long and short) that establish distinct surface distributions. Randomness was modelled by assigning each roughness length scale a randomly generated amplitude and phase shift. Furthermore, roughness amplitudes were scaled using a power law (5.5) that was characterised by a coefficient k, that ensures the

https://doi.org/10.1017/jfm.2021.717 Published online by Cambridge University Press

energy of the PSD was primarily found in the longer roughness wavelengths (Van Deusen 1967). A receptivity formula, based on adjoint perturbation fields, was formulated and used to predict the receptivity or initial amplitude of the stationary cross-flow instability established by surface roughness. The amplitude of the disturbance, generated by surface roughness, is then instantaneously determined by a simple integration of known quantities; normalised adjoint vorticity fields and the roughness shape. Thus, the adjoint approach for receptivity offers huge computational and time advantages over slower LNS based receptivity strategies.

Adjoint perturbation fields, required to predict receptivity, were considerably larger about the radial range that the stationary cross-flow instability first appears. Indeed, receptivity was significantly enhanced by surface roughness located about this annular region. This behaviour is consistent with observations on a swept wing (Radeztsky *et al.* 1999), where the receptivity of stationary cross-flow vortices is strongest near the leading edge.

A Monte-Carlo type uncertainty quantification analysis was undertaken, whereby many thousands of roughness distributions were randomly generated and disturbance amplitudes determined. Receptivity characteristics were averaged over all roughness realisations to compute the expected mean amplitudes and spread. Disturbance amplitudes were noticeably enhanced by roughness distributions that include short roughness scales equivalent to the wavelength of the stationary cross-flow instability. Very short roughness scales, approximately half a cross-flow vortex wavelength and less, were found to have a negligible effect on the receptivity process, which were further diminished as the power law coefficient k increases. Furthermore, mean amplitudes increased significantly for roughness elements fixed about the radial interval $200 \leqslant r \leqslant 400$, while receptivity was less affected by surface roughness located further outboard.

The onset of the nonlinear stage in the laminar–turbulent transition process was estimated by coupling the adjoint predictions for the mean amplitude with the radial growth of the stationary cross-flow instability. The r.m.s. of the roughness was varied to determine the effects on transition brought about by this convectively unstable disturbance. It was assumed that the linear stability assumptions were invalid and nonlinear effects emerged about the radial location that the azimuthal velocity perturbation field attained a magnitude of order 10^{-1}. Results suggest that for relatively large roughness r.m.s. values (greater than 10^{-4}), stationary cross-flow modes $n \leqslant 30$ will achieve the linear–nonlinear threshold first, and thus, will be responsible for the appearance of nonlinear behaviour and engineering transition to turbulence. However, for smaller r.m.s. values that might be more representative of a clean rotating disc, marginally larger cross-flow modes, $n \geqslant 32$, were first to attain the threshold amplitude. Hence, these modes are expected to be significant in bringing about the latter stages of transition on a clean disc, which is consistent with many experimental and numerical observations.

The current investigation focuses on the development of stationary cross-flow disturbances in the infinite rotating disc boundary layer, which are assumed here to be responsible for the early stages of laminar–turbulent transition. The growth of travelling cross-flow waves established by acoustics or free-stream vortex structures, and mechanisms linked to local absolute instability (Lingwood 1995), linear globally unstable disturbances (Thomas & Davies 2018) and disc edge effects (Healey 2010; Imayama *et al.* 2013; Pier 2013; Appelquist *et al.* 2015, 2016) were ignored. For very small roughness r.m.s. values, the absolute route to turbulence may transpire (Imayama *et al.* 2016) as the convectively growing cross-flow instabilities may not achieve sufficiently large amplitudes until further downstream. Additionally, the roughness model imposed in this study was assumed to be periodic in the azimuthal direction. In real experiments,

https://doi.org/10.1017/jfm.2021.717 Published online by Cambridge University Press

roughness will be fully three dimensional and may be localised in both the radial and azimuthal directions. Thus, for future receptivity studies, it will be necessary to extend the simplified two-dimensional model (5.4) to three dimensions, and determine the effect on the receptivity process and disturbance amplitudes. Hence, to ascertain a greater understanding of the transition process on a rotating disc, we suggest that the mean disturbance amplitudes computed herein and from a fully three-dimensional roughness study be used as initial conditions in a fully global nonlinear instability investigation. The radial region that nonlinear effects can be expected to ensue can then be determined more precisely (as opposed to the estimates made above). Furthermore, by combining real profile measurements of a disc surface (made using a profilometer) with the adjoint receptivity formulation, it may be possible to specify the exact PSDs in the roughness model (5.4) and, hence, compute the expected mean disturbance amplitudes for experimental studies on the rotating disc.

Acknowledgements. We are grateful to the referees for several suggestions which have led to a much improved paper.

Declaration of interests. The authors report no conflict of interest.

Author ORCIDs.
Christian Thomas https://orcid.org/0000-0003-4324-530X;
Christopher Davies https://orcid.org/0000-0002-5592-9541.

References

Airiau, C. 2000 Non-parallel acoustic receptivity of a Blasius boundary layer using an adjoint approach. *Flow Turbul. Combust.* **65**, 347–367.

Appelquist, E., Schlatter, P., Alfredsson, P.H. & Lingwood, R.J. 2015 Global linear instability of the rotating-disk flow investigated through simulations. *J. Fluid Mech.* **765**, 612–631.

Appelquist, E., Schlatter, P., Alfredsson, P.H. & Lingwood, R.J. 2016 On the global nonlinear instability of the rotating-disk flow over a finite domain. *J. Fluid Mech.* **803**, 332–355.

Appelquist, E., Schlatter, P., Alfredsson, P.H. & Lingwood, R.J. 2018 Transition to turbulence in the rotating-disk boundary-layer flow with stationary vortices. *J. Fluid Mech.* **836**, 43–71.

Balachandar, S., Streett, C.L. & Malik, M.R. 1992 Secondary instability in rotating-disk flow. *J. Fluid Mech.* **242**, 323–347.

Briggs, R.J. 1964 *Electron-Stream Interactions in Plasmas*. MIT.

Carpenter, M.H., Choudhari, M., Li, F., Streett, C.L. & Chang, C.L. 2010 Excitation of cross-flow instabilities in a swept wing boundary layer. *AIAA Paper* 2010-378.

Chomaz, J.M., Huerre, P. & Redekopp, L.G. 1988 Bifurcations to local and global modes in spatially-developing flows. *Phys. Rev. Lett.* **60**, 25–28.

Choudhari, M. 1993 Boundary-layer receptivity due to distributed surface imperfections of a deterministic or random nature. *Theor. Comput. Fluid Dyn.* **4**, 101–117.

Choudhari, M. 1994 Roughness-induced generation of cross-flow vortices in three-dimensional boundary layers. *Theor. Comput. Fluid Dyn.* **6**, 1–30.

Choudhari, M. & Streett, C.L. 1992 A finite Reynolds-number approach for the prediction of boundary-layer receptivity in localized regions. *Phys. Fluids* A **4**, 2495–2514.

Collis, S.S. & Lele, S.K. 1999 Receptivity to surface roughness near a swept leading edge. *J. Fluid Mech.* **380**, 141–168.

Crouch, J.D. 1992*a* Localized receptivity of boundary layers. *Phys. Fluids* A **4**, 1408–1414.

Crouch, J.D. 1992*b* Non-localized receptivity of boundary layers. *J. Fluid Mech.* **244**, 567–581.

Davies, C & Carpenter, P.W. 2001 A novel velocity-vorticity formulation of the Navier–Stokes equations with applications to boundary layer disturbance evolution. *J. Comput. Phys.* **172**, 119–165.

Davies, C & Carpenter, P.W. 2003 Global behaviour corresponding to the absolute instability of the rotating-disc boundary layer. *J. Fluid Mech.* **486**, 287–329.

Dobrinsky, A. 2002 Adjoint analysis for receptivity prediction. PhD thesis, Rice University.

https://doi.org/10.1017/jfm.2021.717 Published online by Cambridge University Press

DOBRINSKY, A. & COLLIS, S.S. 2000 Adjoint parabolized stability equations for receptivity prediction. *AIAA Paper* 2000-2651.

FALLER, A.J & KAYLOR, R.E 1966 A numerical study of the instability of the laminar Ekman boundary-layer. *J. Atmos. Sci.* **23**, 466–480.

GIANNETTI, F. & LUCHINI, P. 2006 Leading-edge receptivity by adjoint methods. *J. Fluid Mech.* **547**, 21–53.

GOLDSTEIN, M.E. 1983 The evolution of Tollmien–Schlichting waves near a leading edge. *J. Fluid Mech.* **127**, 59–81.

GOLDSTEIN, M.E. 1985 Scattering of acoustic waves into Tollmien–Schlichting waves by small streamwise variations in surface geometry. *J. Fluid Mech.* **154**, 509–529.

GREGORY, N, STUART, J.T. & WALKER, W.S. 1955 On the stability of three-dimensional boundary-layers with application to the flow due to a rotating disk. *Phil. Trans. R. Soc. Lond.* A **248**, 155–199.

HEALEY, J.J. 2010 Model for unstable global modes in the rotating-disk boundary layer. *J. Fluid Mech.* **663**, 148–159.

HILL, D.C. 1995 Adjoint systems and their role in the receptivity problem for boundary layers. *J. Fluid Mech.* **292**, 183–204.

HUERRE, P. & MONKEWITZ, P.A. 1990 Local and global instabilities in spatially developing flows. *Annu. Rev. Fluid Mech.* **22**, 473–537.

HUNT, R.E & CRIGHTON, D.G 1991 Instability of flows in spatially developing media. *Proc. R. Soc. Lond.* A **435**, 109–128.

IMAYAMA, S., ALFREDSSON, P.H. & LINGWOOD, R.J. 2012 A new way to describe the transition characteristics of a rotating-disk boundary-layer flow. *Phys. Fluids* **24**, 031701.

IMAYAMA, S., ALFREDSSON, P.H. & LINGWOOD, R.J. 2013 An experimental study of edge effects on rotating-disk transition. *J. Fluid Mech.* **716**, 638–657.

IMAYAMA, S., ALFREDSSON, P.H. & LINGWOOD, R.J. 2014 On the laminar-turbulent transition of the rotating-disk flow – the role of absolute instability. *J. Fluid Mech.* **745**, 132–163.

IMAYAMA, S., ALFREDSSON, P.H. & LINGWOOD, R.J. 2016 Experimental study of rotating-disk boundary-layer flow with surface roughness. *J. Fluid Mech.* **786**, 5–28.

JACOBS, T.D.B., JUNGE, T. & PASTEWKA, L. 2017 Quantitative characterization of surface topography using spectral analysis. *Surf. Topogr. Metrol.* **5**, 013001.

VON KÁRMÁN, TH. 1921 Über laminare und turbulente Reibung. *Z. Angew. Math. Mech.* **1**, 233–252.

KOBAYASHI, R., KOHAMA, Y. & TAKAMADATE, C. 1980 Spiral vortices in boundary layer transition regime on a rotating disk. *Acta Mechanica* **35**, 71–82.

KOHAMA, Y. 1984 Study on boundary layer transition of a rotating disk. *Acta Mechanica* **50**, 193–199.

LEE, K., NISHIO, Y., IZAWA, S. & FUKUNISHI, Y. 2017 Effects of location of excitation on the spiral vortices in the transitional region of a rotating-disk flow. *Phys. Fluids* **29**, 084106.

LEE, K., NISHIO, Y., IZAWA, S. & FUKUNISHI, Y. 2018 The effect of downstream turbulent region on the spiral vortex structures of a rotating-disk flow. *J. Fluid Mech.* **844**, 274–296.

LINGWOOD, R.J. & ALFREDSSON, P.H. 2015 Instabilities of the von Kármán boundary layer. *Appl. Mech. Rev.* **67**, 030803.

LINGWOOD, R.J. 1995 Absolute instability of the boundary-layer on a rotating-disk. *J. Fluid Mech.* **299**, 17–33.

LINGWOOD, R.J. 1996 An experimental study of absolute instability of the rotating-disk boundary-layer flow. *J. Fluid Mech.* **314**, 373–405.

LINGWOOD, R.J. 1997 On the effects of suction and injection on the absolute instability of the rotating-disk boundary layers. *Phys. Fluids* **9**, 1317–1328.

LUCHINI, P. & BOTTARO, A. 1998 Görtler vortices: a backward-in-time approach to the receptivity problem. *J. Fluid Mech.* **363**, 1–23.

LUCHINI, P. & BOTTARO, A. 2014 Adjoint equations in stability analysis. *Annu. Rev. Fluid Mech.* **46**, 493517.

MACK, L.M. 1985 The wave pattern produced by point source on a rotating disk. *AIAA Paper* 85-0490.

MALIK, M.R. 1986 The neutral curve for stationary disturbances in rotating-disk flow. *J. Fluid Mech.* **164**, 275–287.

MALIK, M.R., WILKINSON, S. & ORSZAG, S.A. 1981 Instability and transition in rotating disk flow. *AIAA J.* **19**, 1131–1138.

MORKOVIN, M.V. 1969 On the many faces of transition. In *Viscous Drag Reduction: Proceedings of the Symposium on Viscous Drag Reduction held at the LTV Research Center, Dallas, Texas, September 24 and 25, 1968* (ed. C.S. Wells), pp. 1–31. Springer.

MUGHAL, S.M. & ASHWORTH, R. 2013 Uncertainty quantification based receptivity modelling of cross-flow instabilities induced by distributed surface roughness in swept wing boundary layers. *43rd AIAA Fluid Dynamics Conference, 2013. AIAA Paper* 2013-3106.

https://doi.org/10.1017/jfm.2021.717 Published online by Cambridge University Press

NG, L.L. & CROUCH, J.D. 1999 Roughness-induced receptivity to cross-flow vortices on a swept wing. *Phys. Fluids* **11**, 432.

OTHMAN, H. & CORKE, T.C. 2006 Experimental investigation of absolute instability of a rotating-disk boundary-layer. *J. Fluid Mech.* **565**, 63–94.

PIER, B. 2003 Finite-amplitude cross-flow vortices, secondary instability and transition in the rotating-disk boundary layer. *J. Fluid Mech.* **487**, 315–343.

PIER, B. 2013 Transition near the edge of a rotating disk. *J. Fluid Mech.* **737**, R1.

PRALITS, J.O. & HANIFI, A. 2003 Optimization of steady suction for disturbance control on infinite swept wings. *Phys. Fluids* **15**, 2756–2772.

PRALITS, J.O., HANIFI, A. & HENNINGSON, D.S. 2002 Adjoint-based optimisation of steady suction for disturbance control in incompressible flows. *J. Fluid Mech.* **467**, 129–161.

RADEZTSKY, R.H., REIBERT, M.S. & SARIC, W.S. 1999 Effect of isolated micronsized roughness on transition in swept-wing flows. *AIAA J.* **37**, 1370–1377.

RAPOSO, H., MUGHAL, S. & ASHWORTH, R. 2018 Acoustic receptivity and transition modeling of Tollmien–Schlichting disturbances induced by distributed surface roughness. *Phys. Fluids* **30**, 044105.

REIBERT, M.S., SARIC, W.S., CARILLO, R.B. & CHAPMAN, K.L. 1996 Experiments in nonlinear saturation of stationary cross-flow vortices in a swept-wing boundary layer. *AIAA Paper* 96-0184.

RUBAN, A.I. 1984 On Tollmien–Schlichting wave generation by sound. In *Laminar-Turbulent Transition. International Union of Theoretical and Applied Mechanics* (ed. V.V. Kozlov), pp. 313–320, Springer, Berlin, Heidelberg.

SARIC, W.S., REED, H.L. & KERSCHEN, E.J. 2002 Boundary layer receptivity to freestream disturbances. *Annu. Rev. Fluid Mech.* **34**, 291–319.

SARIC, W.S., REED, H.L. & WHITE, E.B. 2003 Stability and transition of three-dimensional boundary layers. *Annu. Rev. Fluid Mech.* **35**, 413–440.

SARIC, W.S., CARRILLO, R.B. JR. & REIBERT, M.S. 1998 Leading-edge roughness as a transition control mechanism. *AIAA Paper* 98-0781.

SAYLES, S. & THOMAS, T.R. 1978 Surface topography as a nonstationary random process. *Nature* **271**, 431–434.

SCHRADER, L.U., AMIN, S. & BRANDT, L. 2010 Transition to turbulence in the boundary layer over a smooth and rough swept plate exposed to free-stream turbulence. *J. Fluid Mech.* **646**, 297–325.

SCHRADER, L.U., BRANDT, L. & HENNINGSON, D.S. 2009 Receptivity mechanisms in three-dimensional boundary layer flows. *J. Fluid Mech.* **618**, 209–241.

SIDDIQUI, M.E., MUKUND, V., SCOTT, J. & PIER, B. 2013 Experimental characterization of transition region in rotating-disk boundary layer. *Phys. Fluids* **25**, 034102.

TEMPELMANN, D., HANIFI, A. & HENNINGSON, D.S. 2012*a* Swept-wing boundary layer receptivity. *J. Fluid Mech.* **700**, 490–501.

TEMPELMANN, D., SCHRADER, L.U., HANIFI, A., BRANDT, L. & HENNINGSON, D.S. 2012*b* Swept wing boundary-layer receptivity to localized surface roughness. *J. Fluid Mech.* **711**, 516–544.

THOMAS, C. & DAVIES, C. 2018 On the impulse response and global instability development of the infinite rotating-disc boundary layer. *J. Fluid Mech.* **857**, 239–269.

THOMAS, C. & DAVIES, C. 2019 Global linear instability of rotating-cone boundary layers in a quiescent medium. *Phys. Rev. Fluids* **4**, 043902.

THOMAS, C., MUGHAL, S. & ASHWORTH, R. 2017 On predicting receptivity to surface roughness in a compressible infinite swept wing boundary layer. *Phys. Fluids* **29**, 034102.

THOMAS, C., STEPHEN, S.O. & DAVIES, C. 2020 Effects of partial slip on the local-global linear stability of the rotating disk boundary layer. *Phys. Fluids* **32**, 074105.

VAN DEUSEN, D. 1967 A statistical technique for the dynamic analysis of vehicles traversing rough yielding and non-yielding surfaces. *NASA Tech. Rep.* CR-659, 178 pages.

WILKINSON, S. & MALIK, M.R. 1985 Stability experiments in the flow over a rotating disk. *AIAA J.* **23**, 588–595.

WU, X. 2001*a* On local boundary-layer receptivity to vortical disturbances in the free stream. *J. Fluid Mech.* **449**, 373–393.

WU, X. 2001*b* Receptivity of boundary layers with distributed roughness to vortical and acoustic disturbances: a second-order asymptotic theory and comparison with experiments. *J. Fluid Mech.* **431**, 91–133.

https://doi.org/10.1017/jfm.2021.717 Published online by Cambridge University Press